PHYSICAL REVIEW E **107**, 054136 (2023)

Depinning in the quenched Kardar-Parisi-Zhang class. I. Mappings, simulations, and algorithm

Gauthier Mukerjee,[1] Juan A. Bonachela,[2] Miguel A. Muñoz,[3] and Kay Jörg Wiese[1]
[1]*Laboratoire de Physique de l'École Normale Supérieure, ENS, Université PSL, CNRS, Sorbonne Université, Université Paris-Diderot, Sorbonne Paris Cité, 24 rue Lhomond, 75005 Paris, France*
[2]*Department of Ecology, Evolution, and Natural Resources, Rutgers University, New Brunswick, New Jersey 08901, USA*
[3]*Departamento de Electromagnetismo y Física de la Materia and Instituto Carlos I de Física Teórica y Computacional, Universidad de Granada, Granada 18071, Spain*

(Received 28 July 2022; accepted 20 April 2023; published 30 May 2023)

Depinning of elastic systems advancing on disordered media can usually be described by the quenched Edwards-Wilkinson equation (qEW). However, additional ingredients such as anharmonicity and forces that cannot be derived from a potential energy may generate a different scaling behavior at depinning. The most experimentally relevant is the Kardar-Parisi-Zhang (KPZ) term, proportional to the square of the slope at each site, which drives the critical behavior into the so-called quenched KPZ (qKPZ) universality class. We study this universality class both numerically and analytically: by using exact mappings we show that at least for $d = 1, 2$ this class encompasses not only the qKPZ equation itself, but also anharmonic depinning and a well-known class of cellular automata introduced by Tang and Leschhorn. We develop scaling arguments for all critical exponents, including size and duration of avalanches. The scale is set by the confining potential strength m^2. This allows us to estimate numerically these exponents as well as the m-dependent effective force correlator $\Delta(w)$, and its correlation length $\rho := \Delta(0)/|\Delta'(0)|$. Finally, we present an algorithm to numerically estimate the effective (m-dependent) elasticity c, and the effective KPZ nonlinearity λ. This allows us to define a dimensionless universal KPZ amplitude $\mathcal{A} := \rho\lambda/c$, which takes the value $\mathcal{A} = 1.10(2)$ in all systems considered in $d = 1$. This proves that qKPZ is the effective field theory for all these models. Our work paves the way for a deeper understanding of depinning in the qKPZ class, and in particular, for the construction of a field theory that we describe in a companion paper.

DOI: 10.1103/PhysRevE.107.054136

I. INTRODUCTION

Diverse systems can be modeled as an elastic object (line, surface, manifold) advancing through a random medium with quenched disorder: disordered magnets and the associated Barkhausen noise [1], expanding fronts of bacterial colonies [2,3], systems that show self-organized criticality [4], or coffee soaking into this paper (if you are old fashioned enough to use a printout and to pour your coffee onto it) [5–7]. Often, the elastic system experiences a so-called "depinning transition" as a function of some driving parameter, so that the system changes from being pinned in some configuration to advancing at an average velocity [8]. This phase transition can be thought of as the transition between an active state, where the elastic interface (or surface etc.) changes over time, and an absorbing or quiescent state, where the interface remains frozen [9]. At the transition, the dynamics becomes universal at sufficiently large scales, universality appears as microscopic details are irrelevant, and different systems and models can be grouped together into a few universality classes. The latter can then be studied via the renormalization group (RG) and, more specifically, by employing functional renormalization group (FRG) approaches [10–16].

The simplest prototypical model for depinning transitions is the quenched Edwards-Wilkinson equation (qEW), also called *harmonic depinning*. It monitors the height $u(x,t) \in \mathbb{R}$ of a d-dimensional interface embedded into $d+1$ dimensions. By construction, this excludes overhangs as well as bubbles. Its dynamics is described by

$$\eta\partial_t u(x,t) = \underbrace{c\nabla^2 u(x,t)}_{\text{harmonic elasticity}} + \underbrace{m^2[w-u(x,t)]}_{\text{confinement and driving}} + \underbrace{F(x,u(x,t))}_{\text{pinning forces}}. \tag{1}$$

The pinning forces $F(x,u)$ are quenched Gaussian random variables with variance $\overline{F(x,u)F(x',u')} = \delta^d(x-x')\Delta_0(u-u')$. $\Delta_0(u)$ is the microscopic disorder-force correlator, assumed to decay rapidly for short-range (SR) disorder [8]. The system is driven by slowly increasing w, either as $w = vt$ (with v small) or via a small "kick," $w \to w + \delta w$ whenever the interface is stuck (pinned). The latter protocol is particularly useful to study avalanches [17–34].

While the microscopic force correlator $\Delta_0(u)$ can be analytic, the effective renormalized correlator $\Delta(w)$ seen in the field theory [10–16], and measurable in experiments [35–39] exhibits a cusp at $w = 0$. The slope at the cusp is proportional to the typical avalanche size, $|\Delta'(0^+)| \sim \langle S^2\rangle/\langle S\rangle$ [19].

The qEW class is not the only universality class for interface depinning. As we show here, there is one other rather large universality class, which we will establish is relevant whenever *nonlinear effects cannot be neglected*. As an example, the coffee going into our paper can be modeled by the cellular automaton proposed in 1992 by Tang and Leschhorn (TL92) [40] or variants thereof [41,42]. As it permeates through the paper, the coffee is blocked by a percolating line orthogonal to the coffee front, a phenomenon known as *directed-percolation depinning* (DPD) [5]. At a coarse-grained level one observes that the coffee front tends to grow in its normal direction, inducing anisotropy in the invaded medium. This phenomenon is modeled by an additional term, usually called a *KPZ term* [43], in the equation of motion,

$$\eta\partial_t u(x,t) = \cdots + \underbrace{\lambda[\nabla u(x,t)]^2}_{\text{KPZ-term}}. \tag{2}$$

In addition to fluid invasion (our coffee front) [5–7], experiments on bacterial colonies [2,3] or chemical reaction fronts [44,45] share this property.

In our setup, there is a preferred direction in the medium: the coffee front starts from a flat initial condition. If there is no such preferred direction, or the microscopic disorder is very strong, the critical behavior may be different [46].

Finally, the elastic restoring force may be stronger than the harmonic elasticity in Eq. (1). This is particularly important at depinning in dimension $d = 1$, where the roughness exponent $\zeta = 5/4$ is larger than 1, meaning that the width of the interface grows stronger than the system size. As argued in Ref. [47] this implies that the small-displacement expansion for the elastic energy must be invalid, and one needs to go to the next order and include anharmonic elastic terms to bring the roughness to $\zeta \leqslant 1$. The interpretation in Ref. [47] is that an elastic string would break and the qEW model is unphysical. For domain walls in 2D magnets this leaves two possibilities: either they are self-affine interfaces in the qKPZ class, or non-self-affine (i.e., not described by a height function), and then possibly (isotropic) fractals.

We show below that all these models belong to the same universality class, termed the *quenched Kardar-Parisi-Zhang* (qKPZ) universality class [48]. The field theoretic treatment of qKPZ via FRG is, however, fraught with difficulties [49]. The reason is that in [49] the effective KPZ coupling λ generically flows to strong coupling, indicating that the perturbative treatment breaks down. Reference [49] further contained a subspace of fixed points defined by closed RG equations. This subspace is characterized by an exponentially decaying effective force correlators $\Delta(w)$. Our study was motivated by the observation that such a fixed point is indeed realized for the pair-contact process (PCP) [50]. However, our numerical simulations indicate that none of the models discussed above have an exponentially decaying $\Delta(w)$. A field theory that agrees with the simulations is therefore needed.

In view of the theoretical problems, here we tackle the system first numerically and use the results to guide development of the theory. The first key conceptual advance is the introduction of a confining potential proportional to m^2. When $m^2 = \infty$, the interface position is the flat configuration $u(x,t) = w$. As a consequence, both the elastic term $c\nabla^2 u(x,t)$ and the KPZ term $\lambda[\nabla u(x,t)]^2$ vanish. Thus when we sample the total forces acting on the interface, and its correlations $\Delta(w)$ (see Sec. V), we see the microscopic correlations $\Delta_0(w)$ of $F(x,u)$. Let us now decrease m^2. As the interface explores more configurations and takes advantage of stronger pinning configurations, the total pinning force increases, while at the same time the interface becomes wider. Viewing the dynamics as a function of w, the size of jumps increases (with decreasing m), while their rate decreases. This leads to larger correlation lengths ξ_m in the x direction and $\xi_\perp$ in the driving direction.

While we can take m smaller and smaller, we cannot take $m = 0$ to start with, as we cannot even define a steady state. However, when ξ_m surpasses the system size, its effect on the (spatial) correlations of $u(x)$ becomes invisible. Thus for all practical purposes, we have reached the scaling limit.

Apart from the effective (total) force correlator $\Delta(w)$, we numerically estimate the flow of the parameters c and λ as a function of the confining potential strength m^2, to assess whether the effective nonlinearity λ flows to infinity as it did in the field theory of [49] or reaches a fixed point. In the latter scenario, we could hope to be able to *repair* the field theory. Our overall goal is to identify the *effective* field theory, i.e., the effective large-scale theory, without having to resort to field theory techniques, such as a diagrammatic expansion.

Our second key advance is to construct an algorithm to estimate all parameters of the effective field theory, as a function of m. Our conclusion is that an effective field theory with finite, m-dependent parameters exists, and it has the form of the qKPZ equation. More specifically, we define a dimensionless effective KPZ amplitude $\mathcal{A}$,

$$\mathcal{A} := \lim_{m\to 0} \frac{\lambda}{c}\rho, \tag{3}$$

where λ is the KPZ nonlinearity in Eq. (2), c the effective elasticity in Eq. (1), and ρ the correlation length of the effective force correlator (for a precise definition see Sec. V G). Since the limit in Eq. (3) exists, the theory remains valid for the more common setting of the qKPZ equation without an m^2 term. $\mathcal{A}$ should be viewed as the effective KPZ nonlinearity in dimensionless units: It vanishes in qEW, and we show numerically that $\mathcal{A}$ is the same for the TL92 cellular automaton, qKPZ, and anharmonic depinning. This supports our claim that (at least in $d = 1, 2$) there is only one universality class with $\mathcal{A} \neq 0$ which differs from qEW with $\mathcal{A} = 0$. The qKPZ fixed point is relevant even if the deviations from qEW in the microscopic model are small.

This paper is organized as follows: in Sec. II we describe the models we use. We then show through mappings that these models are in the same universality class (Sec. III). Section IV is devoted to a scaling analysis, with the confining potential m^2 defining our class of exponents. How to estimate numerically the effective field theory is described in Sec. V, first for the force correlator (Secs. V B-V C) and then the coupling constants (Secs. V E–V G). Brief conclusions are offered in Sec. VI. In a companion paper [51] we show how to obtain the effective field theory from a diagrammatic approach.

II. MODELS

In this section we define three models. The first two are described by a continuous equation, while the third one is a cellular automaton model, i.e., a discrete microscopic model. We show in Sec. III that they can all be mapped onto each other.

A. QKPZ equation

The quenched KPZ equation (qKPZ) is defined as

$$\eta\partial_t u(x,t) = c\nabla^2 u(x,t) + \lambda[\nabla u(x,t)]^2 + m^2[w - u(x,t)] + F(x,u(x,t)). \quad (4)$$

Rescaling u and $F(x,u)$, we could set $\lambda \to 1$. We prefer to not rescale the disorder, and thus λ will change under RG. Invariant under these transformations is the sign of λv, i.e., λ times the driving velocity $v = dw/dt$. A positive sign defines what is called the positive qKPZ equation. The negative qKPZ equation exhibits a very different phenomenology, with the propagating front spontaneously generating facets [44,52,53].

Discretization of the KPZ term [second term on the r.h.s. of Eq. (4)] is not trivial, and the choice made for it is important. We use the discretization of Ref. [54],

$$\begin{aligned} u(x,t+\delta t) - u(x,t) &= \delta t \Bigg\{ m^2[w - u(x,t)] + F(x,u(x,t)) \\ &\quad + c[u(x+1,t) + u(x-1,t) - 2u(x,t)] \\ &\quad + \lambda\left[\frac{u(x+1,t) - u(x-1,t)}{2}\right]^2 \Bigg\} \\ &\text{with } \lambda = 3, \quad c = 1, \quad \delta t = 0.01. \end{aligned} \quad (5)$$

Our main control parameter m is varied between 0.05 and 0.6. The system size is chosen to be $L \leqslant 512$ with L the linear size. Following standard approaches, the disorder forces are drawn from a Gaussian distribution with unit variance, linearly interpolated between integer values of u. While efficient algorithms exists for the other two models, a direct simulation of the qKPZ equation is computationally expensive, and we have restricted our simulations to $d = 1$.

B. Anharmonic depinning

Anharmonic depinning (aDep) is defined by the equation

$$\eta\partial_t u(x,t) = \underbrace{c_4\nabla\cdot\left\{\nabla u(x,t)[\nabla u(x,t)]^2\right\}}_{\text{anharmonic elasticity}} + \underbrace{c\nabla^2 u(x,t)}_{\text{harmonic elasticity}} + \underbrace{m^2[w - u(x,t)]}_{\text{driving force}} + \underbrace{F(x,u(x,t))}_{\text{quenched disorder}}. \quad (6)$$

If $\vec{e}_i$ represents the unit vectors in d dimensions, the discretized anharmonic energies are

$$\mathcal{H}_{\rm el}[u] = \sum_x \sum_{i=1}^d \mathcal{E}_{\rm el}[u(x+\vec{e}_i) - u(x)], \quad (7)$$

$$\mathcal{E}_{\rm el}(u) = \frac{c}{2}u^2 + \frac{c_4}{4}u^4. \quad (8)$$

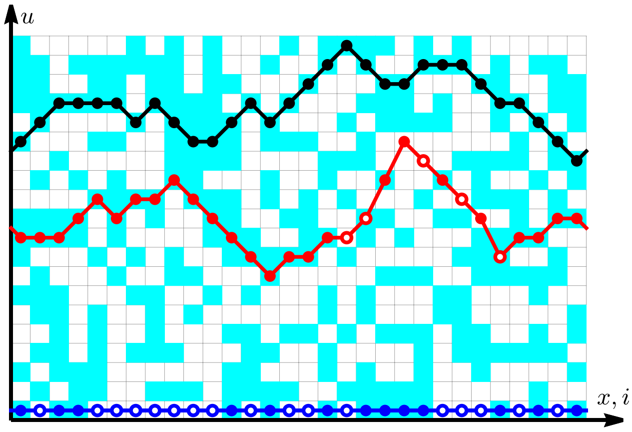

FIG. 1. The cellular automaton TL92. Blocking cells, i.e., cells above the threshold are drawn in cyan; those below in white. The initial configuration is the string at height 1 (dark blue). The interface moves up. An intermediate configuration is shown in red, the final configuration in black. Open circles represent unstable points, i.e., points which can move forward; closed circles are stable.

The resulting elastic forces at site x are

$$\begin{aligned} -\frac{\delta\mathcal{H}_{\rm el}[u]}{\delta u(x)} &= \sum_i \mathcal{E}'_{\rm el}[(u(x+\vec{e}_i) - u(x)] + \mathcal{E}'_{\rm el}[u(x-\vec{e}_i) - u(x)] \\ &= c\sum_{i=1}^d [u(x+\vec{e}_i) + u(x-\vec{e}_i) - 2u(x)] \\ &\quad + c_4\sum_{i=1}^d [u(x+\vec{e}_i) - u(x)]^3 + [u(x-\vec{e}_i) - u(x)]^3. \end{aligned} \quad (9)$$

The discretizations are similar to the qKPZ equation. For $d = 1$, we simulate systems with size up to $L = 2048$, assuming $m \leqslant 0.05$. Using GPUs in $d = 2$ allowed us to reach $L = 256$, with $m = 0.09$. In $d = 3$, we reached $L = 64$, and $m = 0.08$. To speed up simulations, we set $c = 0$, after checking that it gives the same results as $c = 1$. We varied the anharmonic term as $c_4 = 0.1, 0.2, 0.3$. There are 6×10^5 ($d = 1$), 5×10^4 ($d = 2$), and 2×10^4 ($d = 3$) independent samples. By construction, this system only moves forward, respecting the Middleton “no-passing” theorem [55]; see Sec. III A. This allows us to use the very efficient algorithm introduced in Ref. [56].

C. TL92

To describe fluid imbibition, Tang and Leschorn introduced the cellular automaton visualized in Fig. 1 (TL92) [40]. On a square lattice, each cell (i, j) is assigned a variable $f(i, j) \in [0, 1]$. If $f(i, j) < p$ the cell is considered closed (blocking). Otherwise the cell is considered open. The interface starts from a flat configuration at the bottom (dark blue on Fig. 1). A point $(i, j = u_i)$ on this interface is unstable and can move forward by 1, $u_i \to u_i + 1$, according to the following rules (in that order):

(i) Links cannot be longer than two. If a site is two cells ahead of its neighbors, stop.

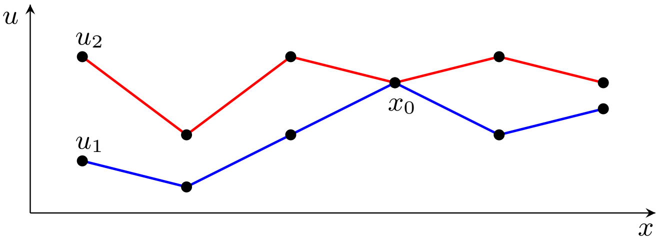

FIG. 2. Two configurations at depinning.

(ii) If $f(i, j) > p$, move forward.

(iii) If one of the neighboring sites is two cells ahead, move forward.

While in the original version the critical force p is a constant [40], here we choose it to depend on the height $j = u_i$ of the interface,

$$p := m^2(u_i - w). \tag{10}$$

This has two consequences: first, as $f(i, j) \in [0, 1]$, rule (ii) is satisfied for all $u_i < w$, and never satisfied for $u_i > w + m^{-2}$. As a result, the interface is trapped in a domain of size m^{-2}. Increasing w, we can drive the interface as in qEW, Eq. (1). Our protocol is to keep w fixed until a stable configuration is reached, and only then increase w by δw. Two timescales are thus separated: a fast one governing the reorganization of the system, and an infinitely slower one corresponding to the driving. We use this protocol to calculate the effective force correlator and to simulate avalanches.

The interface is pinned when all its cells are blocking; its maximal slope is 1; see Fig. 1. This ensures that a directed-percolation path goes from left to right, i.e., perpendicular to the driving direction [40]. To be precise, the line gets pinned at the lowest percolating cluster (see Fig. 4). This relation to directed percolation allows us to use many of the high-precision results available for DP (see Sec. IV D). Since time in the DP formulation is from left to right, whereas time for depinning of an interface is in the u direction, this correspondence is restricted to static quantities i.e., those corresponding to blocking configurations.

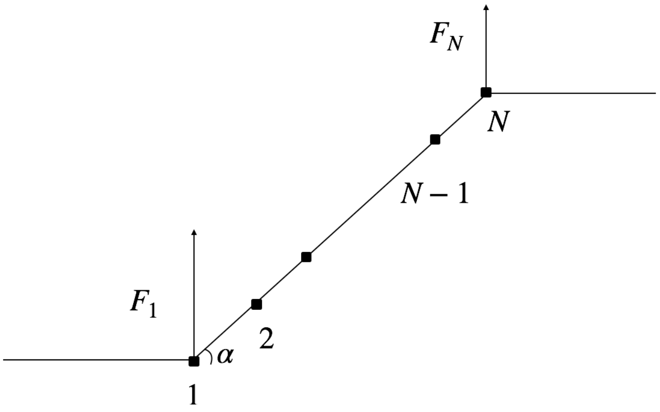

FIG. 3. Possible instability of the qKPZ equation, when a series of locally aligned points have a slope α. The interface goes back to being flat at large distance, due to the $\xi_\perp/\xi_m \to 0$. The force felt by the lowest point is greater than the force felt by the lowest point. Below a certain slope α, this configuration does not generate a local slope above α.

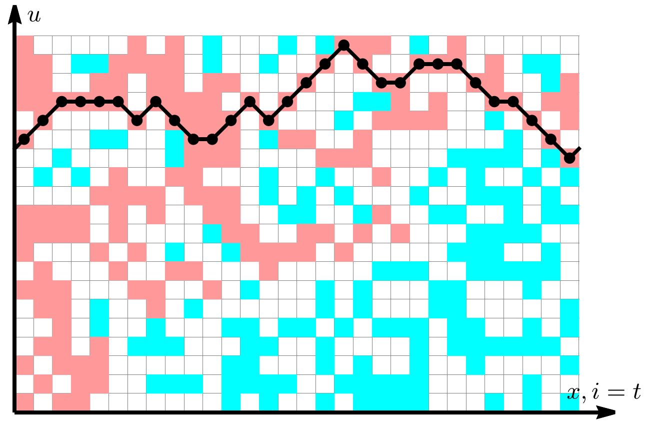

FIG. 4. Directed percolation from left to right. A site (i, u) is defined to be *connected* if it is occupied and at least one of its left neighbors $(i-1, u)$, $(i-1, u \pm 1)$ is connected. The index i takes the role of time t.

In our simulations of this cellular automaton, we use $L = 4096$ and $m \geqslant 0.02$ in $d = 1$. GPU computing allows us to reach $L = 256$ at $m = 0.05$ in two dimensions and $L = 128$ and $m = 0.1$ in three.

III. MAPPINGS

In this section we present different mappings between the three models introduced in Secs. II A to II C. Some of these mappings rely on no-passing theorems, which we prove below first.

A. No-passing theorems for TL92 and anharmonic depinning

In parallel to the famous no-passing theorem by Middleton [55] for harmonic depinning, we now prove a similar theorem for TL92 and anharmonic depinning.

1. No-passing theorem for anharmonic depinning in the continuum

Assumptions

The elastic energy between nearest neighbors $\mathcal{E}(u)$ in Eq. (8) is a convex function,

The disorder force $F(x, u)$ is continuous in u,

$\dot{u}(x, t) \geqslant 0$.

No-Passing Theorem I (depinning in the continuum)

$\dot{u}(x, t') \geqslant 0$ for all $t' \geqslant t$.

If two configurations are ordered, $u_2(x, t) \geqslant u_1(x, t)$, then they remain ordered for all times, i.e., $u_2(x, t') \geqslant u_1(x, t')$ for all $t' > t$.

Proof. Consider an interface discretized in x. The trajectories $u(x, t)$ are a function of time. Suppose that there exists x and $t' > t$ such that $\dot{u}(x, t') < 0$. Define t_0 as the first time when this happens, $t_0 := \inf_x \inf_{t'>t}\{\dot{u}(x, t') < 0\}$, and x_0 the corresponding position x. By continuity of F in u, the velocity $\dot{u}$ is continuous in time, and $\dot{u}(x_0, t_0) = 0$. This implies that the disorder force acting on x_0 does not change in the next (infinitesimal) time step, and the only changes in force can come from a change in the elastic terms. Since by assumption no other point has a negative velocity and the elastic energy $\mathcal{E}(u)$ is convex, this change in force cannot be negative, contradicting the assumption.

To prove the second part of the theorem, consider the following configuration at time t_0: Here the red configuration is ahead of the blue one, except at position x_0, where they coincide. As in the first part of the proof, we wish to bring to a contradiction the hypothesis that at some later time $u_1(x_0)$ (blue in Fig. 2) is ahead of $u_2(x_0)$ (red). For this reason, we have chosen t_0 the infimum of times contradicting the theorem, $t_0 := \inf_{t'>t}\{u_1(x_0,t') > u_2(x_0,t')\}$. Consider the equation of motion for the difference between u_1 and u_2 at point x_0. According to Eqs. (6) and more generally (9),

$$\begin{aligned}\eta\partial_t[u_2(x_0,t) - u_1(x_0,t)]\big|_{t=t_0} &= \sum_{x=\mathrm{nn}(x_0,t_0)} \mathcal{E}'_{\rm el}[u_2(x,t_0) - u_2(x_0,t_0)] \\ &\quad - \mathcal{E}'_{\rm el}[u_1(x,t_0) - u_1(x_0,t_0)] \\ &\geqslant 0. \end{aligned} \tag{11}$$

The sum runs over all nearest neighbors of x_0. The disorder forces have canceled as well as the term of order m^2, since by assumption $u_2(x_0,t_0) = u_1(x_0,t_0)$. The inequality follows from monotonicity of $\mathcal{E}'_{\rm el}(u)$, equivalent to the convexity of $\mathcal{E}(u)$.

2. *No-passing theorem for anharmonic depinning as a cellular automaton*

Assumptions

The positions $u(x,t)$ are integers; they can grow by 1 in an update, or remain constant.

The elastic energy between nearest neighbors $\mathcal{E}(u)$ is convex.

No-Passing Theorem II (Cellular Automaton for Depinning)

If two configurations are ordered, $u_2(x,t) \geqslant u_1(x,t)$, then they remain ordered for all times, i.e., $u_2(x,t') \geqslant u_1(x,t')$ for all $t' > t$.

Proof. As for theorem I.

3. *No-passing theorem for TL92*

No-Passing Theorem III (TL92)

If two configurations are ordered, $u_2(x,t) \geqslant u_1(x,t)$, then they remain ordered for all times, i.e., $u_2(x,t') \geqslant u_1(x,t')$ for all $t' > t$.

Proof. Consider again point x_0 on Fig. 2. By direct inspection of all possible configurations one shows that either nobody moves, red and blue move together, or only red moves. This works as well for parallel update as for single-site update, provided one updates both configurations at the same time.

B. Mapping from anharmonic depinning to TL92

1. *General idea*

The general idea is to show that, *for an appropriate choice of parameters*, both TL92 and anharmonic depinning have the same blocking configurations. This statement has two directions:

A blocking configuration for TL92 is a blocking configuration for the depinning of an elastic line.

All other configurations move forward.

We failed to prove the stronger statement, namely, that each site stable in an allowed TL92 configuration is also stable for depinning, and that only allowed TL92 configurations appear at depinning. This means that the dynamics of both models may be different, and even show different dynamical critical exponents.

2. *Cellular automaton in $d = 1$*

We aim to find the blocking configurations of TL92 with an interface whose law of evolution is the one of anharmonic depinning as given in Eq. (6), at least with a specific choice of parameters. To that end, we need to check for a given disorder that every configuration of the interface following the anharmonic depinning equation stops at the same configuration as in TL92. Let us start with a cellular automaton version. We choose disorder forces $F = \pm 1$, where $F = 1$ corresponds to open sites, and $F = -1$ to blocking sites. The height is integer, and whenever a site is unstable, it is moved ahead by 1, as in TL92. Whether a site moves or not depends only on its relative position to its nearest neighbors. Therefore, we only need to test whether there is agreement for 25 configurations: the two neighbors of a site can be separated by a distance with values in $\{-2, -1, 0, 1, 2\}$. The maximum distance is given by the TL92 rule that two neighbors cannot be separated by a distance of more than 2, a condition anharmonic depinning needs to satisfy too. Symmetry of the forces under the exchange of the left and right neighbors decreases the number of distinct cases to 15. If one can find parameters c and c_4, such that the two prescriptions agree on those 15 configurations, the anharmonic depinning equation agrees for any interface configuration with TL92, and we have our mapping.

For each configuration to be tested, there are three sites to check: the left, the middle, and the right ones. We note the relative position of the left and right neighbors: for example, $(+1, +1)$ corresponds to a "v" shape with slope 1, $(-2, +2)$ to "/" with slope 2, and so on. Our considerations are for the middle point. If according to the TL92 rules it moves, the force felt by it must be $\geqslant 0$, otherwise $\leqslant 0$. The discretization of the equation of motion is given in Eq. (9), with elastic forces between two neighbors $c_4(u_i - u_{i+1})^3$. This gives the inequalities in Table I. With one exception, they are fulfilled by taking $c_4 \in]\frac{1}{7}, \frac{1}{2}[$; a centered value of $c_4 = 1/4$ is a good choice. Then in all cases anharmonic depinning has the same update rules as TL92, except for the configuration $(2, -2)$, a strongly inclined line. We did not succeed in tweaking the model such that this configuration is also always stable at depinning. On the other hand, all blocking TL92 configurations are also blocking at depinning, and there is no configuration blocked at depinning which would move in TL92.

Using the no-passing theorems II and III shows that both models have exactly the same blocking configurations, and that they are chosen independently from the history. Since anharmonic depinning can move faster than TL92, we conclude

TABLE I. Conditions on the anharmonic depinning coefficients, such that anharmonic depinning evolves as TL92, for each of the configurations in TL92.

Configuration	Condition	Configuration	Condition
(2,2)	$16c_4 > 1$	$(1, -2)$	$7c_4 > 1$
(2,1)	$9c_4 > 1$	(0,0)	True
(2,0)	$8c_4 > 1$	$(0, -1)$	$-1 < c_4 < 1$
$(2, -1)$	$7c_4 > 1$	$(0, -2)$	$8c_4 > 1$
$(2, -2)$	False	$(-1, -1)$	$-1 < 2c_4 < 1$
(1,1)	$-1 < 2c_4 < 1$	$(-1, -2)$	$9c_4 > 1$
(1,0)	$-1 < c_4 < 1$	$(-2, -2)$	$16c_4 > 1$
$(1, -1)$	True		

that their corresponding dynamical exponents should satisfy

$$z_{\mathrm{TL92}} \geqslant z_{\mathrm{aDep}}. \tag{12}$$

3. Cellular automaton in an arbitrary dimension

We now generalize our considerations to an arbitrary dimension d. We first derive necessary conditions for a (globally) blocking configuration in TL92:

(i) A blocking configuration of TL92 has no site whose neighbor is at a distance -2.

(ii) A blocking configuration of TL92 has no site whose neighbor is at a distance 2.

As (ii) is trivial, we only need to prove (i): Suppose a site s_1 exists with a neighbor s_2 at a distance -2. Then their heights $u(s)$ satisfy

$$u(s_2) = u(s_1) - 2. \tag{13}$$

If site s_2 has a neighbor s_3 which is at a height distance -2, we continue to s_3, and so on. Since $u(s_i)$ is a decreasing sequence, and the minimum of all heights $u_{\min} := \min_s u(s)$ exists, this process stops, say, at step n. By construction site s_n has no neighbor at distance -2, but at least neighbor s_{n-1} at distance 2. Thus site s_n is unstable, proving (i).

Let us now check for each site s its local configuration $l_s = (\delta u_1, \ldots, \delta u_{2d})$, defined as in Sec. III B 2. We start with a globally blocking configuration in TL92. Due to (i) and (ii), all its $\delta u_i \in \{-1, 0, 1\}$. Whether the site is stable or not is *disorder decided*. We have to ensure that this is the same for anharmonic depinning. To simplify matters, we set $c \to 0$, only retaining c_4. In TL92 the site is unstable if $F = 1$ and stable if $F = -1$. Let us consider the stable case. In order to reproduce this in anharmonic depinning, we need that even if all neighbors pull in the opposite direction, i.e., are 1, the site remains stable. This implies the

(iii) Condition from configuration $l_s = (1, 1, \ldots, 1)$:

$$c_4 < \frac{1}{2d}. \tag{14}$$

If the site in TL92 is unstable, the same condition arises, this time for the configuration $(-1, -1, \ldots, -1)$.

Next consider a configuration with one -2:

(iv) Condition from $l_s = (-2, \ldots)$: none.

TL92 is blocked, while aDep may move or not. Due to the no-passing theorems, nothing has to be checked.

It remains to check a configuration with at least one 2:

(5) Condition from $l_s = (2, \ldots)$:

$$c_4(9 - 2d) > 1. \tag{15}$$

Proof. We need aDep to move. The worst case is that the disorder is $F = -1$, and that all remaining neighbors pull backwards. Since we have already excluded case (iv), they can maximally be at a distance -1. This gives the condition that the total elastic force $c_4[2^3 - (2d - 1)] > 1$. Simplifying yields Eq. (15).

We conclude that TL92 and aDep always find the same blocking configurations (in $d \leqslant 4$), as long as

$$\frac{1}{9 - 2d} < c_4 < \frac{1}{2d}. \tag{16}$$

This gives the bounds

$$\tfrac{1}{7} < c_4^{d=1} < \tfrac{1}{2}, \tag{17}$$

$$\tfrac{1}{5} < c_4^{d=2} < \tfrac{1}{4}. \tag{18}$$

In $d = 3$ there is no solution, but one can repeat the argument with an anharmonicity

$$\mathcal{E}_{\mathrm{el}}(u) = \frac{c_{2p}}{2p} u^{2p}. \tag{19}$$

While the bound (14) remains valid as a condition for c_{2p}, Eq. (15) changes to

$$c_{2p}(2^{2p-1} + 1 - 2d) > 1. \tag{20}$$

Therefore the simplest solution in $d = 3$ reads

$$\tfrac{1}{27} < c_6 < \tfrac{1}{6}. \tag{21}$$

This leaves open the possibility that in $d = 3$ several anharmonic-depinning universality classes exist. Both our simulations and the literature [5] are in favor of that hypothesis.

4. Depinning in the continuum

In [8] (Sec. 5.7) a continuum model was proposed in $d = 1$ which finds the blocking configurations of TL92, and otherwise moves. The idea is to let the disorder act only close to integer values of u, and to provide a sufficiently strong force in between. This way anharmonic depinning stops at TL92 configurations, but never in between.

C. Mapping qKPZ to TL92

The mapping of qKPZ onto TL92 is more delicate as qKPZ has no no-passing theorem. In Table II we show the conditions to be satisfied for a cellular-automaton version of qKPZ, termed qKPZc. Inspection shows that not all conditions can be satisfied simultaneously. This remained true if we enlarged the space of allowed models. As an example, we allowed for an additional constant term in the equation of motion.

What we could achieve, however, is that blocking configurations of TL92 are blocking for qKPZc, while most of the nonblocking configurations of TL92 are nonblocking for qKPZc, choosing

$$c = \tfrac{2}{5}, \quad \lambda = \tfrac{1}{2}. \tag{22}$$

TABLE II. Set of conditions on the qKPZ coefficients for each possible configuration in TL92. $F = 1$ is the maximum disorder force. We can satisfy most conditions by choosing $c = 2/5$, $\lambda = 1/2$, as indicated by the check marks.

TL92 blocking			TL92 nonblocking		
Configuration	Condition		Configuration	Condition	
(1,1)	$c < \frac{1}{2}$	✓	(2,2)	$c > \frac{1}{4}$	✓
(1,0)	$c + \frac{\lambda}{4} < 1$	✓	(2,1)	$3c + \frac{\lambda}{4} > 1$	✓
$(1, -1)$	$\lambda < 1$	✓	(2,0)	$2c + \lambda > 1$	✓
(0, 0)	True	✓	$(2, -1)$	$4c + 9\lambda > 4$	✓
$(0, -1)$	$-1 < c - \frac{\lambda}{4} < 1$	✓	$(2, -2)$	$1 + 4\lambda < 0$	
$(-1, -1)$	$c < \frac{1}{2}$	✓	$(1, -2)$	$4 + 9\lambda < 4c$	
			$(0, -2)$	$1 + \lambda < 2c$	
			$(-1, -2)$	$4 + \lambda < 12c$	✓
			$(-2, -2)$	$c > \frac{1}{4}$	✓

The violating cases $(2, -2)$, $(1, -2)$, and $(0, -2)$ do not move in TL92, but move in qKPZc, bringing us out of the allowed configurations of TL92.

We now provide heuristic arguments that in the continuous version these configurations are not reached. In the continuum and close to the depinning transition, we have $\frac{\xi_\perp}{\xi_m} \to 0$. As a result, at large distances compared to the lattice cutoff but below the correlation length ξ_m, the interface must be flat on average. Now suppose that a series of sites are aligned and has the maximal available slope α. This extremal perturbation is shown in Fig. 3. We use the discretization of Eq. . We do not consider the disorder for simplicity. (It enters in this argument only through the structure of the space swept by the interface between avalanches.) If we name F_1 the force felt by the leftmost site of the slope, and F_N the force felt by the rightmost of the slope, then (independent of the KPZ term)

$$\Delta F_{1N} = F_N - F_1 = -2c\alpha. \tag{23}$$

As a result globally the perturbation gets flattened. For $i \in \{2, 3, \dots, N-2\}$ we have $\Delta F_{i,i+1} = 0$. And finally

$$\Delta F_{12} = -\alpha c + \frac{3\lambda\alpha^2}{4}, \tag{24}$$

$$\Delta F_{N-1,N} = -\alpha c - \frac{3\lambda\alpha^2}{4}. \tag{25}$$

The local slope does not increase if $\alpha \leqslant \frac{4c}{3\lambda}$. With the previous values for λ and c this gives $\alpha \leqslant \frac{16}{15}$. So while we expect slope $\alpha = 1$ to be commonly reached, larger slopes are not. As a result, the configurations $(2, -2)$ and $(1, -2)$ are not reached, and that their associated conditions are not fulfilled does not matter. Finally, for the case $(-2, 0)$, it corresponds to the highest site of the perturbation. We can see from Eq. (25) that it always experiences a force that is weaker than the site just below, and as a result the local slope gets flattened and cannot reach the value $(-2, 0)$. Adding disorder is statistically more likely to pin the site N, which feels a weaker forward force, than the site 1, accelerating the smoothening of the perturbation. We checked by numerical simulations of Eqs. (5) and in $d = 1$, with forces set to $F = 1$ for an open cell, and $F = -1$ for a blocking cell, and $c = \frac{2}{5}$, $\lambda = \frac{1}{2}$ that qKPZ stops at the same blocking configuration as TL92.

TABLE III. All scaling relations derived in this paper. $\nu_\perp$, $\nu_\parallel$ come from DP mappings.

$\xi_\perp \sim \xi_\parallel^\zeta$,	$\zeta = \frac{\nu_\perp}{\nu_\parallel}$,	$\zeta_m = \frac{2\nu_\perp}{1+\nu_\perp}$,
$\frac{\zeta_m}{\zeta} = \nu_\parallel(2 - \zeta_m)$,	$\xi_m = Cm^{-\frac{\zeta_m}{\zeta}}$,	$\beta = \frac{\zeta_m(z-\zeta)}{\zeta(2-\zeta_m)}$,
$\Psi_\eta = z\frac{\zeta_m}{\zeta} - 2$,	$\Psi_c = 2\frac{\zeta_m - \zeta}{\zeta}$,	$\Psi_\lambda = 2\frac{\zeta_m - \zeta}{\zeta} - \zeta_m$,
$\tau = 2 - \frac{2}{d\frac{\zeta_m}{\zeta} + \zeta_m}$,	$(1-\tau)\frac{d+\zeta}{z} = 1 - \alpha$.	

D. Mapping anharmonic depinning to qKPZ

Starting from the anharmonic-depinning Eq. (6), the KPZ term is generated under renormalization, even in the limit of a vanishing driving velocity, $v \to 0^+$, which corresponds to depinning, under the combined action of the anharmonicity and the nonanalytic disorder force correlator. This was shown in [49] and is reproduced in the companion paper [51]. The KPZ term generated is then more *relevant*, in the renormalization-group sense, than the anharmonic elastic terms. This ensures that anharmonic depinning belongs to the qKPZ class.

IV. CRITICAL EXPONENTS AND SCALING RELATIONS

Some scaling relations have already been derived [5,40,41], using the distance to the critical point as a control parameter. However, in order to construct the field theory, one has to introduce an infrared regularization acting in the x direction. This is achieved by driving the surface using a confining potential with strength m^2, i.e., the term $m^2[w - u(x,t)]$ in Eqs. (1), (4), and (6) and $m^2[u_i - w]$ in Eq. (10). It is this term which forbids rare large fluctuations in the u direction. Moreover, this term is crucial for the field theory to have a fixed point [51], to estimate the effective-force correlations (see Sec. V below), and to quantitatively compare the RG flow between field theory and simulations. It is thus necessary to derive all scaling relations in terms of the confining potential strength m^2 or *mass* m. While the m dependence in correlation functions disappears for $\xi_m \gtrsim L$, having a finite (even tiny) m allows us to be in the steady state. All scaling relations are summarized in Table III.

A. Why use a confining potential of strength m^2?

The reader may wonder why we use a protocol with a confining potential of strength m^2, as in Eqs. (1) and (4)–(6) There are several reasons: First of all, this allows us to reach a steady state, and not only to approach it, as is the case when tuning an applied force to the depinning threshold. Second, having an energetically preferred position w allows us to talk about fluctuations of the center of mass u_w around w. Finally, as discussed in Sec. V, this allows us to measure correlations of the effective force.

It is important that the confining-potential strength m^2 is protected, i.e., changes with scale m as m^2 (without any correction): On average the center of mass u_w of the interface follows the driving term w, i.e., $m^2\overline{[u_w - w]} = f_c$. If one changes $w \to w + \delta w$, this results in an increase in force $\delta f = m^2 \delta w$, and the center of mass in the long-time limit

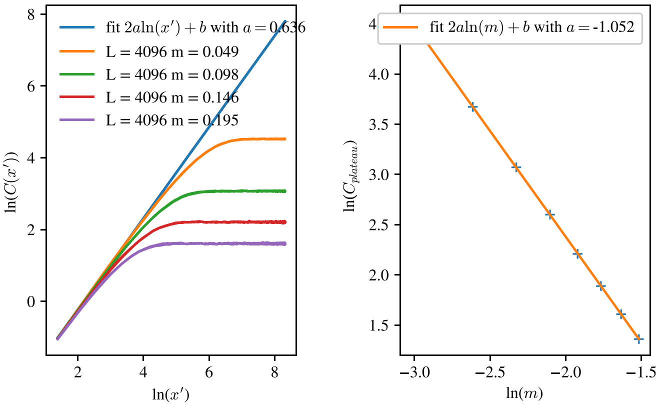

FIG. 5. (Left) TL92 1D two-point function $C(x)$ for different values of m (not all shown here), plotted against $x' = \frac{4x(L-x)}{L}$ to take advantage of the periodic boundary conditions. We read off the exponent $\zeta = 0.636$ in the linear part of the curve (the slope is 2ζ). (Right) Scaling of the plateau of the two-point functions for different m. The fit yields $\zeta_m = 1.052$.

is $u_w \to u_w + \delta w$, on average. As a result, the long-time response of the center of mass to a change of force δf is $1/m^2$. Since this holds both on the microscopic and macroscopic level, the effective m^2 is the same as the microscopic one.

B. Correlation lengths

There are two correlations lengths for the interface. One is in the direction parallel to the interface $\xi_\parallel$, the other in the perpendicular direction $\xi_\perp$. They are both due to the confining potential, i.e., m^2, but we name the parallel correlation length $\xi_m = \xi_\parallel$, because it is the long-distance cutoff set by m. We will place ourselves in the regime where the long-distance (infrared) cutoff is not given by the system size L but by ξ_m. We define the *roughness exponent* ζ as the exponent characterizing the scaling of the lengths in the perpendicular direction with respect to the lengths in the parallel direction. At short distances $u \sim x^\zeta$ (see Fig. 5), which translates into a relation between the two correlation lengths

$$\xi_\perp \sim \xi_m^\zeta. \tag{26}$$

The scaling properties of both qEW and qKPZ can be expressed as a function of ξ_m.

1. Scaling of ξ_m and $\xi_\perp$ for qEW

In qEW the parameters c and m are protected by a symmetry, called the statistical tilt symmetry [8]. As a result, c does not acquire an anomalous dimension under renormalization, and thus does not depend on m and ξ_m. At depinning, all forces scale in the same way, so equating the elastic force with the driving we get

$$\begin{aligned} \nabla^2 u &\sim m^2 u \\ \Rightarrow \xi_m &\sim m^{-1}. \end{aligned} \tag{27}$$

From Eq. (26) we obtain

$$\xi_\perp \sim m^{-\zeta}. \tag{28}$$

2. Scaling of ξ_m, $\xi_\perp$ for qKPZ

In qKPZ the term $\lambda(\nabla u)^2$ breaks the statistical tilt symmetry. As a consequence, c is no longer protected and acquires an anomalous dimension. Only m is protected (see Sec. IV A). Assuming again that at depinning all forces scale in the same way,

$$\begin{aligned} c\nabla^2 u &\sim m^2 u \\ \Rightarrow \xi_m &\sim \frac{\sqrt{c}}{m}. \end{aligned} \tag{29}$$

As we show below, c increases when $m \to 0$. As a result, the system has a larger correlation length than in qEW. Now that ξ_m has a nontrivial scaling, we need an exponent to describe this scaling. We chose to use the scaling of $\xi_\perp$ with m, defining

$$\xi_\perp \sim m^{-\zeta_m}. \tag{30}$$

Using Eq. (26) we obtain

$$\xi_m \sim m^{-\frac{\zeta_m}{\zeta}}. \tag{31}$$

C. Definition of the two-point function

The two-point function is defined as

$$\begin{aligned} C(x-y) &:= \frac{1}{2}\overline{[u(x) - u(y)]^2} \\ &\sim \begin{cases} A|x-y|^{2\zeta}, & |x-y| \ll \xi_m \\ Bm^{-2\zeta_m}, & |x-y| \gg \xi_m \end{cases}. \end{aligned} \tag{32}$$

The average is taken over disorder configurations. We can formally define $\xi_\perp$ as

$$\xi_\perp^2 := C(x-y)|_{|x-y|\gg\xi_m}. \tag{33}$$

$\xi_\parallel = \xi_m$ is the intersection point between the two asymptotic behaviors. Taking $x = \xi_m$ in the two-point function, we get $A\xi_m^{2\zeta} \simeq Bm^{-2\zeta_m}$, and as a consequence

$$\xi_m = Cm^{-\frac{\zeta_m}{\zeta}}, \quad C = \left(\frac{B}{A}\right)^{\frac{1}{2\zeta}}. \tag{34}$$

Let us stress that key features of this universality class stem from $\frac{\zeta_m}{\zeta} \neq 1$. This is illustrated with numerical results for the TL92 automaton in $d = 1$ in Fig. 5, and for $d = 2$ in Fig. 6. For anharmonic depinning Figs. 7 and 8 show results in dimensions $d = 2$ and $d = 3$. Before we discuss them in depth, let us extract the critical exponents in $d = 1$ from directed percolation. This will serve as a strong check on our simulations.

D. Connection to directed percolation

In Sec. III we discussed that blocking configurations in TL92 are paths in directed percolation. Here we extract the exponents ζ and ζ_m from DP exponents. As the latter are known precisely [9,57,58], we get precise predictions for the former.

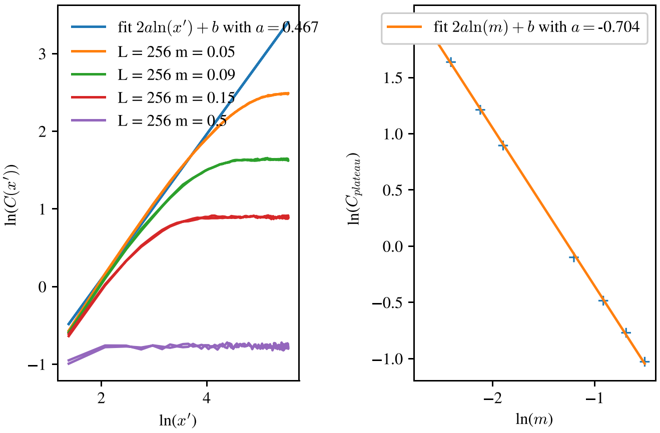

FIG. 6. (Left) TL92 2D two-point function $C(x)$ along the diagonal of the system for different values of m (not all shown) plotted against $x' = \frac{4x\sqrt{2}(L\sqrt{2}-x\sqrt{2})}{\sqrt{2}L}$. The exponent $\zeta \approx 0.47$ is obtained from the linear part of the curve. (Right) Scaling of the plateau of the two-point functions for different m. The fit yields $\zeta_m = 0.70$.

There are two guiding principles for these relations: all forces at depinning have the same scaling dimension, and every length parallel to the interface scales as x or ξ_m, while lengths in the perpendicular direction scale as $u \sim x^{\zeta} \sim m^{-\zeta_m}$.

Consider Fig. 4 which shows directed-percolation paths from left to right (in pink). They are constructed on a square lattice, where occupied cells (in pink or cyan) are selected with probability p, and the remaining once are unoccupied (white). A cell (i, j) is said to be connected to the left boundary (and colored pink) if it is occupied, and if at least one of its three neighbors $(i-1, j)$ and $(i-1, j\pm 1)$ is connected to the left boundary. The system is said to percolate if at least one point on the right boundary is connected to the left boundary. To achieve periodic boundary conditions for TL92, it is further required that this remains true for the periodically continued system.

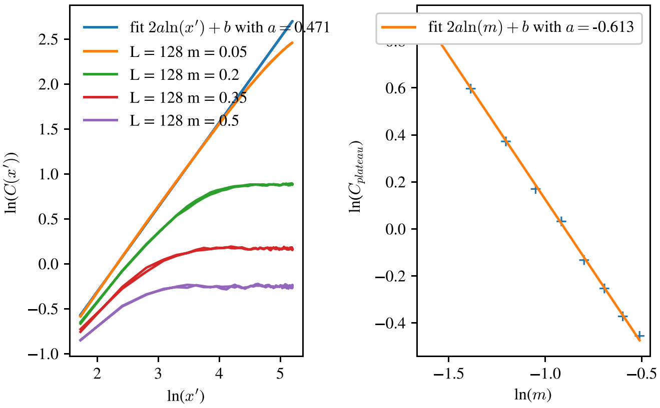

FIG. 7. (Left) Anharmonic depinning 2D two-point function $C(x)$ alongside the diagonal of the system for different values of m (not all shown here) plotted against $x' = \frac{4x\sqrt{2}(L\sqrt{2}-x\sqrt{2})}{\sqrt{2}L}$. The exponent $\zeta = 0.47$ is extracted from the linear part of the curve. (right) Scaling of the plateau of the two-point functions for different m. The fit gives $\zeta_m = 0.61$.

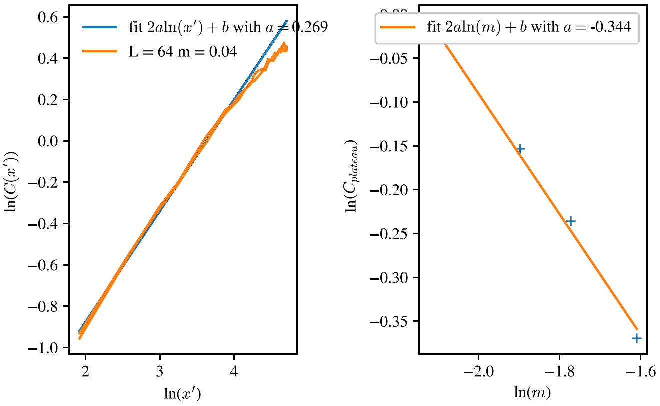

FIG. 8. (Left) Anharmonic depinning 3D two-point function $C(x)$ alongside the diagonal of the system for different values of m (not all shown) plotted against $x' = \frac{4x\sqrt{3}(L\sqrt{3}-x\sqrt{3})}{\sqrt{3}L}$. The exponent $\zeta = 0.27$ is read off from the linear part of the curve. (Right) Scaling of the plateau of the two-point functions for different m. The fit gives $\zeta_m = 0.34$.

While percolation is unlikely for small p, it is likely for large p, with a transition at $p = p_c$. There are three independent exponents β, $\nu_\parallel$, and $\nu_\perp$, defined via

$$\rho(t) := \left\langle \frac{1}{h} \sum_u s_u(t) \right\rangle \xrightarrow{t\to\infty} \rho^{\rm stat}, \tag{35}$$

$$\rho_{\rm stat} \sim (p - p_c)^{\beta}, \quad p > p_c, \tag{36}$$

$$\xi_\parallel = |p - p_c|^{-\nu_\parallel}, \tag{37}$$

$$\xi_\perp = |p - p_c|^{-\nu_\perp}. \tag{38}$$

Here $s_u(t)$ is the *activity* of site u at time t, set to one if the site is connected to the left boundary, and zero otherwise. $h = \sum_u$ is the height of the system, and $\rho_{\rm stat}$ the stationary density of active sites. $\xi_\parallel$ is the size of the DP cluster along the parallel (time) direction, and $\xi_\perp$ the size in the transverse direction.

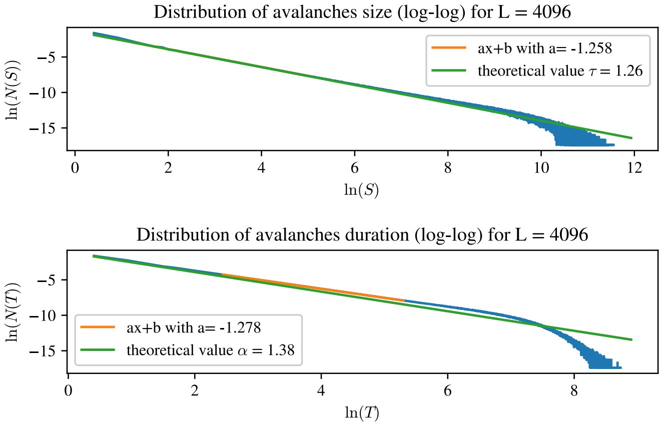

FIG. 9. Avalanche size and duration distributions for TL92. τ and α are the associated exponents. We also computed S_m and T_m from these distributions at different m and verified the relations (51) and (55) (not shown).

TABLE IV. Critical exponents ζ and ζ_m of the qEW and qKPZ classes, from simulations of anharmonic depinning and comparison with the literature. Only ζ was measured in the literature, while ζ_m is also necessary to describe the qKPZ class (see Sec. IV B 2).

Model	ζ	ζ_m	ζ literature
aDep 1D	0.635(6)	1.054(3)	0.63 [47]
TL92 1D	0.636(8)	1.052(5)	0.63 [5]
qKPZ 1D	0.64(2)	1.05(1)	0.633 (8) [54]
qEW 1D	1.25(1)	1.25(1)	1.25 [47,60,61]
aDep 2D	0.48(2)	0.61(2)	0.45 (1) [47]
TL92 2D	0.47(3)	0.70(3)	0.48 (3) [5]
qEW 2D	—	—	0.753 (2) [47]
TL92 3D	0.44(5)	0.52(6)	0.38 (4) [5]
aDep 3D	0.27(4)	0.34(4)	0.25 (2) [47]
qEW 3D	—	—	0.355 (1) [47]

The last two relations imply

$$\xi_\perp \sim \xi_\parallel^\zeta \Rightarrow \zeta^{d=1} = \frac{\nu_\perp}{\nu_\parallel} = 0.632613(3). \tag{39}$$

This is the roughness exponent ζ defined in Eq. (32). All numerical values are collected in Table V.

For TL92, the surface is blocked by directed percolation paths in the direction parallel to the interface (from left to right). However, instead of a global p, we have a u-dependent p, given by $p - p_c = m^2(u - w)$. As a result, the distance to p_c in DP corresponds to a driving force in TL92. Together with $u \simeq \xi_\perp \sim (p - p_c)^{-\nu_\perp}$, this gives $m^2 \sim (p - p_c)^{1+\nu_\perp}$ or $(p - p_c) \sim m^{\frac{2}{1+\nu_\perp}}$. This finally yields

$$u \sim m^{-\zeta_m} \Rightarrow \zeta_m^{d=1} = \frac{2\nu_\perp}{1 + \nu_\perp} = 1.046190(4). \tag{40}$$

Note that in contrast to qEW (where $\zeta_m = \zeta$), here $\zeta_m > \zeta$.

TABLE V. The DP values for all exponents are from Ref. [9] (first two lines), combined with the scaling relations derived here (following lines). The agreement between the static exponents numerically estimated for aDep and TL92 and their DP values is excellent. There is no such mapping for dynamical exponents. The conjecture $z = 1$ advanced in Ref. [5] is in contradiction to our simulations; see Appendix A for a detailed discussion.

Exponent	DP value	Simulated value
$\nu_\parallel$	1.733847(6)	
$\nu_\perp$	1.096854(4)	
ζ	0.632613(3)	0.636(4)
ζ_m	1.046190(4)	1.052(6)
$\frac{\zeta_m}{\zeta}$	1.65376(1)	1.65(1)
τ	1.259246(3)	1.257(5)
ψ_c	1.30752(2)	1.31(4)
ψ_λ	0.26133(2)	0.28(3)
z	—	1.10(2)
α	—	1.28(3)
ψ_η	—	−0.18(1)
β	—	0.81(3)

In $d \geqslant 2$ directed-percolation paths are 1D, whereas the interface is d-dimensional. As a result, the mapping breaks down and one has to introduce directed surfaces [59]. Since no information for our simulations is gained, we will not discuss this case.

E. Results for the two-point function, ζ and ζ_m

For TL92 in $d = 1$, the two-point function is shown in Fig. 5. $d = 2$ is covered in Figs. 6 and 7, while Fig. 8 is for dimension $d = 3$. The results for the critical exponents ζ and ζ_m are summarized in Table IV.

Let us first discuss our choice of simulation parameters. To obtain ζ, the smallest possible m is chosen, such that there is no system-spanning avalanche. The latter would mix the physics of the d-dimensional interface with that of a single degree of freedom. For ζ_m one needs a value of m that allows to clearly see the plateau of the two-point function. Finally, we saw with seemingly little noise the two-point function for larger systems, until $L = 1024$ for TL92, but we found systematic errors in those bigger systems, due to a lack of statistics. As a rule of thumb, 2×10^4 avalanches/per site are necessary to ensure a scaling collapse of the two-point function for different sizes.

Let us now discuss our results, summarized on Tables IV and V. In $d = 1$, there are consistent values for ζ and ζ_m between the three simulated models and directed percolation. We thus have confirmed numerically that there is a single universality class, and that the scaling arguments for ζ (known in the literature) and ζ_m (introduced here) are valid.

In $d = 2$, our simulations show that TL92 and anharmonic depinning share the same exponents. This is consistent with the mapping established in Sec. III B 3.

In $d = 3$, the exponents seemingly differ, suggesting that the two universality classes may be different. This is consistent with the absence of a mapping established at the end of Sec. III B 3. On the other hand, we cannot exclude that finite-size corrections, which are expected to be large for a cellular automaton such as TL92, are responsible for this lack of agreement.

F. The exponent ν

By definition of the correlation-length exponent $\nu_\parallel$, $\xi_m \sim (f - f_c)^{-\nu_\parallel}$, with f the driving force, and f_c the critical depinning force. This identifies the standard depinning exponent ν as

$$\nu^{d=1} = \nu_\parallel. \tag{41}$$

Since $(f - f_c) = m^2(u - w) \sim m^{2-\zeta_m}$, together with Eq. (31) this implies

$$\frac{\zeta_m}{\zeta} = \nu(2 - \zeta_m). \tag{42}$$

This relation is valid in any dimension $d \leqslant d_c$ and does not rely on the mapping to DP. In $d = 1$ replacing ζ_m and ζ by their expressions in terms of $\nu_\perp$ and $\nu_\parallel$ given in Sec. IV D, we verify consistency.

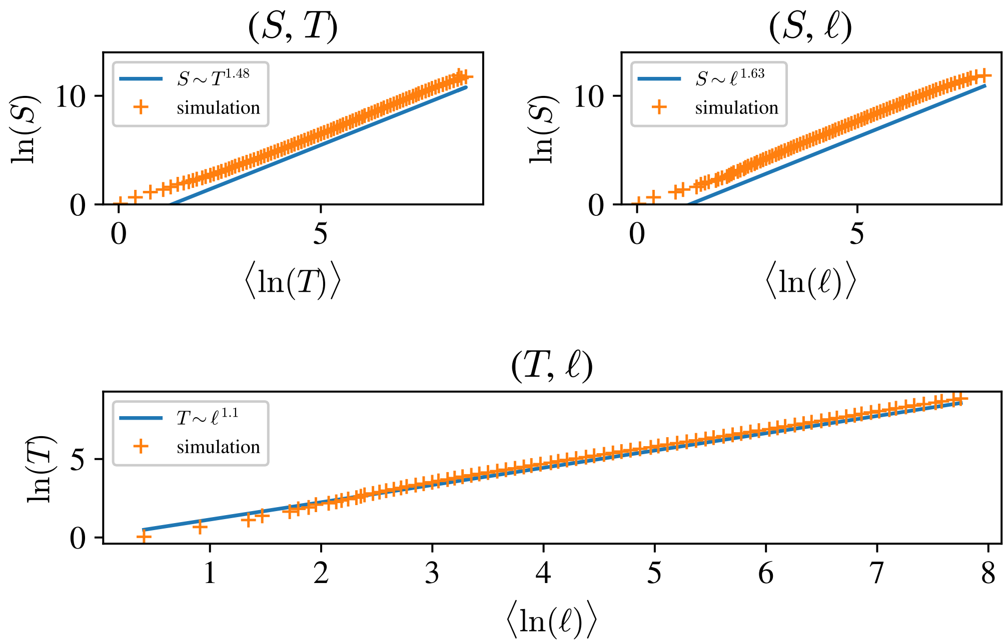

FIG. 10. Joint probability distributions of $(S, \langle T\rangle)$, $(S, \langle \ell\rangle)$, $(T, \langle \ell\rangle)$ in TL92, in log scale, for $d = 1$, for $L = 4096$ and $m = 0.024$. They verify Eqs. (54) and (50) and the definition of z in Eq. (47). Averaging before or after taking the log gives similar results. The solid line is the theoretical prediction.

G. Dynamical exponent *z*

The response function $R(x, t)$ is defined as the response of the system at time t and position x, given a kick in the force of the confining potential $m^2 w(x, t)$ at time $t = 0$ and $x = 0$ (we use translational invariance in both space and time),

$$R(x,t) := \frac{\delta\langle u(x,t)\rangle}{m^2\delta w(0,0)}. \qquad (43)$$

Assume that the response function takes the scaling form

$$R(x,t) = \frac{1}{m^2 t^{\frac{d}{z}}} f\left(\frac{x}{t^{\frac{1}{z}}}\right), \qquad (44)$$

where $\int_x f(x) = 1$. Then z is the dynamical critical exponent.

For the velocity of an avalanche by definition $v \sim (f - f_c)^{\beta}$, and $v = \frac{u}{t} = \frac{\xi_\perp}{\xi_\parallel^z} = \xi_\parallel^{\zeta - z} = (f - f_c)^{-\nu_\parallel(\zeta - z)}$. Eliminating $\nu_\parallel$ with the help of Eq. (42) we get

$$\beta = \frac{\zeta_m(z-\zeta)}{\zeta(2-\zeta_m)}. \qquad (45)$$

Scaling relations for qEW are recovered by setting $\zeta_m = \zeta$, resulting in

$$\beta_{\rm qEW} = \frac{z-\zeta}{2-\zeta} = \nu(z-\zeta). \qquad (46)$$

We evaluated z in the TL92 automaton in $d = 1$ by looking at the joint distribution of avalanche duration T and lateral extension ℓ, shown in Fig. 10 (see Sec. IV I for details). Using

$$T \sim \ell^z, \qquad (47)$$

we find

$$z_{\rm TL92}^{d=1} = 1.10 \pm 0.02. \qquad (48)$$

This value contradicts Ref. [5], which conjectures the *exact* value $z = 1$ using heuristic arguments and evidence from numerical simulations. Our simulation, like theirs, computes the lateral extension of an avalanche as a function of its duration. While Ref. [5] extracts the power law by a fit to one decade, we have data on more than 2.5 decades, allowing for a much more precise value. We reviewed the argument given in Ref. [5], which relies on shortest paths on a percolation cluster. Our main criticism is that transport properties on percolation clusters are linked to the proportion of singly connected bonds, bonds that if cut, separate the percolation cluster into two parts (the "blobs and links" representation [62]). Even if the perpendicular direction is small compared to the longitudinal one, it is nonzero, which changes the proportion of singly connected bonds. Details are given in Appendix A.

H. Avalanche size

Let us recall scaling for avalanches, adapted to qKPZ. This is summarized in Table VI. Let S the size of an avalanche, i.e., is the number of sites that are affected in an avalanche (in a cellular automaton), or the volume swept through by

TABLE VI. Scaling relations for qEW can be obtained from qKPZ by setting $\zeta_m = \zeta$. To pass from qEW to qKPZ, it suffices to replace d by $d\frac{\zeta_m}{\zeta}$ and ζ by ζ_m when it is linked to a length in the u direction.

qEW	qKPZ
$\xi_m \sim m^{-1}$	$\xi_m \sim m^{-\frac{\zeta_m}{\zeta}}$
$S_m \sim m^{-d-\zeta}$	$S_m \sim m^{-d\frac{\zeta_m}{\zeta}-\zeta_m}$
$\tau = 2 - \frac{2}{d+\zeta}$	$\tau = 2 - \frac{2}{d\frac{\zeta_m}{\zeta}+\zeta_m}$

the interface between two blocking configurations. Define its typical size S_m as [20]

$$S_m := \frac{\langle S^2 \rangle}{2\langle S \rangle}. \tag{49}$$

If the avalanche-size distribution decays as an exponential for large S, then this exponential decay is $\sim e^{-S/(4S_m)}$ [20,63,64], identifying S_m as the large-scale cutoff. Note that using Eq. (49) is very precise, while fitting a tail is rather imprecise.

Scaling implies that

$$S \sim \ell^{d+\zeta} \quad \Rightarrow \quad S_m \sim \xi_m^{d+\zeta}, \tag{50}$$

where ℓ is the lateral extension of an avalanche. Injecting Eq. (31) yields

$$S_m \sim m^{-d\frac{\zeta_m}{\zeta} - \zeta_m}. \tag{51}$$

Assume that $P_S(S) \sim S^{-\tau}$ for $S \ll S_m$. To obtain a scaling relation for τ, follow [27] to consider the avalanche-size distribution per unit force,

$$\rho_f(S) := \frac{\delta N(S)}{\delta f} \simeq S^{-\tau} f_S(S/S_m) g_S(S/S_0), \quad S_0 \ll S_m. \tag{52}$$

S_m is the large-scale cutoff introduced above, while S_0 is a small-scale cutoff. We expect Eq. (52) to have a finite limit when $m \to 0$ [27]. Associated to a force increase by δf is a total displacement $\int_x \delta u(x) = \langle S \rangle$. The total increase in force can be written as $\delta f = \int_x m^2 \delta u(x) = m^2 \langle S \rangle$. By the definition of ρ_f we have $\langle S \rangle = \delta f \int_0^\infty S \rho_f(S)\, dS$. This gives

$$1 = m^2 \big[S_m^{2-\tau} - O\big(S_0^{2-\tau}\big) \big].$$

Since $\tau < 2$, we can take the limit of $S_0 \to 0$, resulting in

$$\tau = 2 - \frac{2}{d\frac{\zeta_m}{\zeta} + \zeta_m}. \tag{53}$$

We compare this result to simulations in Sec. IV J below.

I. Avalanche duration

Consider the dynamics of an avalanche, with ℓ its lateral extension and T its duration. Using $T \sim \ell^z$ and $S \sim \ell^{d+\zeta}$, we get

$$S \sim T^{\frac{d+\zeta}{z}}. \tag{54}$$

Assume that

$$P_T(T) \sim T^{-\alpha} \quad \text{for } T \ll T_m := \frac{\langle T^2 \rangle}{2\langle T \rangle}. \tag{55}$$

Scaling implies that $P_S(S)dS \sim P_T(T)dT$. For small avalanches (but bigger than the discretization cutoff) this implies that $S^{1-\tau} \sim T^{1-\alpha}$. Using Eq. (54) we obtain

$$\alpha = 1 + \frac{1}{z}\left(d + \zeta - \frac{2\zeta}{\zeta_m} \right). \tag{56}$$

J. Numerical simulations for size and duration

Let us first explain our choice of parameters: to study avalanches, it is important to avoid triggering two overlapping avalanches; to that end, we use a driving strength $w \to w + \delta w$ such that the probability that a site gets depinned is $\frac{1}{40}$. As a comparison, in the other simulations we generate on average one avalanche per driving event. Next, m should be large enough to avoid system-spanning avalanches. For $L = 4096$ we computed our distributions for 2×10^7 avalanches and $m = 0.0244$.

We verified the scaling relations for the dynamic exponent z and the size and duration exponents τ and α. To this end, we recorded for TL92 in $d = 1$ the joint distribution of (S, T, ℓ), with ℓ the lateral extension of the avalanche. This allowed us to extract three joint distributions involving two variables, and shown on Fig. 10. First, we use $T \sim \ell^z$ to extract z in $d = 1$ as

$$z^{d=1} = 1.10(2). \tag{57}$$

This gives for the remaining relations the numerical values $T \sim \ell^{1.48(3)}$ and $S \sim \ell^{1.6326(3)}$. A glance in Fig. 10 shows that the data are in good agreement with these values.

Figure 9 shows the size and duration distributions, with predicted exponents $\tau = 1.2592(6)$, and $\alpha = 1.385(7)$. While the former is satisfied over almost three decades, the latter seemingly comes out much smaller, namely, at

$$\alpha_{\mathrm{TL92}}^{d=1} = 1.28(2). \tag{58}$$

Let us discuss possible sources for this discrepancy:

(i) The real functional form of P_T is more complicated than the scaling anzatz in Eq. (55), and has a "shoulder" that pushes the apparent exponent down. This phenomenon was described for the size distribution P_S in qEW, both numerically [18] and within the FRG [19]; it was studied numerically for P_S on qKPZ [63]. As the top plot of Fig. 9 shows, there is a small shoulder for P_S, but the agreement on the exponent is very good. If the shoulder for P_T is much longer, it is hard to see in Fig. 9.

(ii) We still see large finite-size corrections due to the discretization of the time evolution. This would be surprising in view of the excellent scaling in the (T, ℓ) and (S, T) plots of Fig. 10.

We could properly simulate avalanche durations only in a cellular automaton, since for anharmonic depinning we used the variant Monte Carlo algorithm of [47,65], which has a different (probably faster) time evolution. Whether this amounts to a smaller exponent z is, however, doubtful.

K. Comparison with qEW

What is the effect of the nonlinearity on the physics of the system? Can one get an intuition? The increase of the short-range elasticity with the scale has two main effects: the roughness exponent ζ decreases from 1.25 for qEW to $\zeta = 0.63$ for qKPZ, meaning the width is reduced at large scales. The parallel correlation length ξ_m for $m \to 0$ grows faster than for qEW, reflected in $\frac{\zeta_m}{\zeta} > 1$. As the elasticity at large scales gets stronger, more sites are correlated and the correlation length increases. The avalanche size exponent τ goes from $\tau_{\mathrm{qEW}} = 1.11$ [29] in $d = 1$, to $\tau = 1.26$, close to the one in dimension $d = 2$ for qEW.

V. EFFECTIVE FORCE CORRELATOR $\Delta(w)$ AND RUNNING COUPLING CONSTANTS

A. Definition of the effective force correlator $\Delta(w)$

In Eqs. (1), (4), and (6) we introduced a restoring force $m^2[w - u(x,t)]$ from a confining potential. This was not only necessary to drive the system, but also to estimate the effective force correlator $\Delta(w)$, by measuring the fluctuations of the center-of-mass position u_w of the interface. Define $\Delta(w)$ as

$$\Delta(w-w') := m^4 L^d\, \overline{(u_w - w)(u_{w'} - w')}^{\,c}, \tag{59}$$

$$u_w := \frac{1}{L^d}\int_x u_w(x), \tag{60}$$

$$u_w(x) := \lim_{t\to\infty} u(x,t) \text{ given } w \text{ fixed.} \tag{61}$$

In our protocol, w is increased in steps. One then waits until the interface stops, which defines $u_w(x)$. Its center-of-mass position is u_w, and its fluctuations define $\Delta(w)$.

B. Scaling of $\Delta(w)$

The definition (59) has a finite limit for fixed m, when $L \to \infty$. Using that $u \sim m^{-\zeta_m}$, and that L/ξ_m is dimensionless leads together with Eq. (31) to

$$\Delta(0) \sim m^{4-d\frac{\zeta_m}{\zeta}-2\zeta_m}. \tag{62}$$

For the argument of $\Delta(w)$, we expect

$$w \sim u \sim m^{-\zeta_m}. \tag{63}$$

A nontrivial check is as follows: As in qEW, one can connect the typical avalanche size given in Eq. (49) to the disorder force correlator [see, e.g., [8], Eq. (104)],

$$|\Delta'(0^+)| = m^4 \frac{\langle S^2\rangle}{2\langle S\rangle} \sim m^{4-\zeta_m(d/\zeta+1)}. \tag{64}$$

This is consistent with Eqs. (62) and (63).

C. Measuring $\Delta(w)$

$\Delta(w)$ is defined from the variable u_w in Eq. (61). For depinning, be it anharmonic or not, integrating the equation of motion with periodic boundary conditions leads to

$$m^2(u_w - w) = F_w, \tag{65}$$

$$F_w := \frac{1}{L^d}\int_x F(x, u_w(x)). \tag{66}$$

Thus $\Delta(w)$ is also the correlator of the disorder acting on the interface. This direct connection breaks down in qKPZ, as after integration over the center of mass three terms remain: $m^2(w - u_w)$, F_w, and Λ_w, defined by

$$\Lambda_w := \frac{1}{L^d}\int_x \lambda[\nabla u_w(x)]^2. \tag{67}$$

A configuration at rest then has

$$m^2(w - u_w) + F_w + \Lambda_w = 0. \tag{68}$$

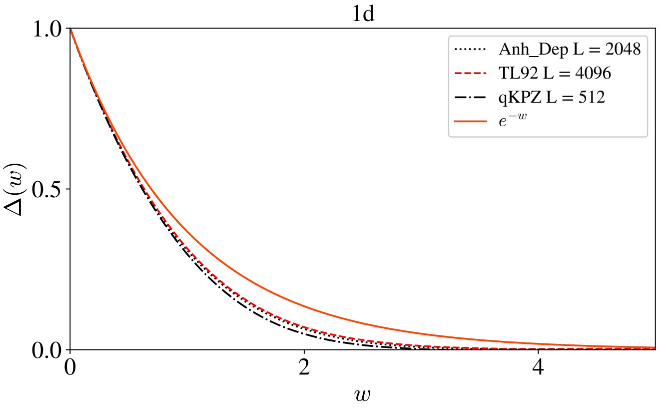

FIG. 11. Comparison of the shapes of the correlators in $d = 1$ and for anharmonic depinning, TL92 and qKPZ with the exponential behavior observed in a subspace in Ref. [49]. We clearly see the following. (a) The correlators for TL92, aDep and qKPZ are very close. (b) The subspace found in [49] is not the one attained by the evolution of those models. The shapes have been normalized by setting $|\Delta'(0^+)| = \Delta(0) = 1$.

We note that while the first and last terms are positive, the middle term is negative. So why did we define $\Delta(w)$ as the (connected) correlations of u_w and not F_w? After all, we call it the *renormalized force correlator*. The answer comes from more sophisticated field theory arguments, developed in a companion paper [51]. In essence it looks at all two-time contributions to the uu correlations and then amputates the external response functions. The result is as given in Eq. (59). For details we refer to [51].

We have verified that Eqs. (62)–(64) hold for TL92 and the other two models. The correct regime to obtain a good scaling collapse for the correlator, with the exponents given in Table IV, is when the infrared cutoff is set by the confining parabola, meaning that the plateau of the two-point function is reached. The results for the shape of $\Delta(w)$ are summarized in Figs. 11 and 12, where everything is rescaled such that $|\Delta'(0^+)| = \Delta(0) = 1$.

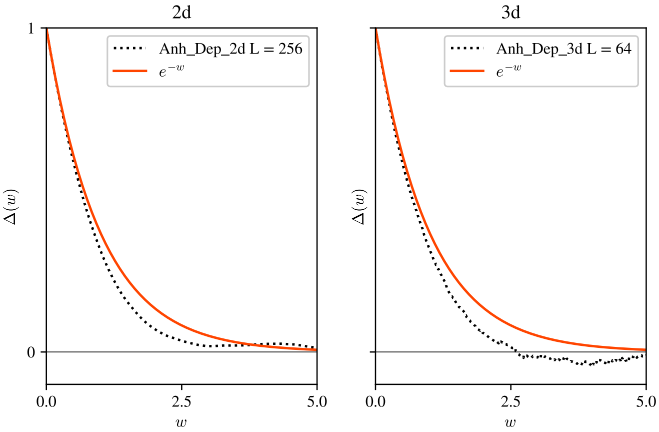

FIG. 12. Comparison of the shapes of the correlators in $d = 2, 3$ for anharmonic depinning with the exponential behavior found for a subspace in Ref. [49]. We see that this subspace is not the one attained by these models. The shapes are normalized such that $|\Delta'(0^+)| = \Delta(0) = 1$.

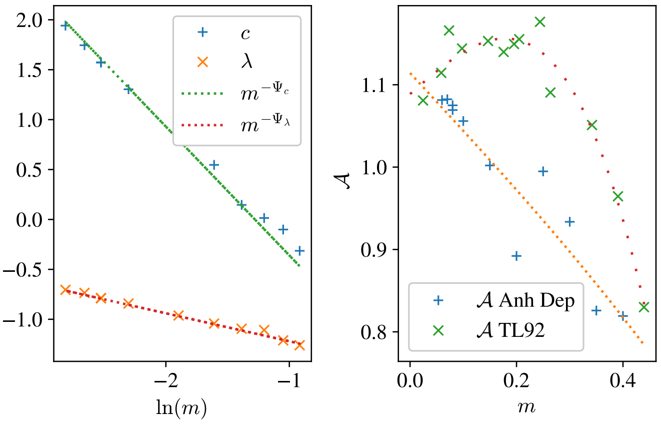

FIG. 13. Left: Double-logarithmic plot for scaling of c and λ for anharmonic depinning in $1d$ as a function of m. Right: Measured amplitude ratios $\mathcal{A}$ for TL92 and anharmonic depinning (linear plot). The dotted lines are guides for the eye. The second-order polynomial fits show convergence to $\mathcal{A} \approx 1.10(2)$ for $m \to 0$.

D. Anomalous dimensions for c, λ, and η

If there were no corrections to c, λ, and η, the theory would be trivial. Before we show in the next Sec. V E an algorithm to estimate their scale dependence, let us first derive their anomalous dimensions, given the information already obtained.

Let us define their scaling dimensions as

$$\lambda \sim m^{-\psi_\lambda}, \tag{69}$$

$$c \sim m^{-\psi_c}, \tag{70}$$

$$\eta \sim m^{-\psi_\eta}. \tag{71}$$

Equating the dimensions of driving force and elasticity, $c\nabla^2 u \sim m^2 u$, we get $m^{-\psi_c-\zeta_m}\xi_m^{-2} \sim m^{2-\zeta_m}$ and together with Eq. (31)

$$\psi_c = 2\frac{\zeta_m - \zeta}{\zeta}. \tag{72}$$

A similar argument for λ yields

$$\psi_\lambda = 2\frac{\zeta_m - \zeta}{\zeta} - \zeta_m. \tag{73}$$

These two relations have been verified (see left of Fig. 13), due to the algorithm we describe in Sec. V E.

The scaling relation for ψ_η is obtained from $\eta\partial_t u \sim m^2 u$, implying $t \sim m^{-2-\psi_\eta} \sim x^{(2+\psi_\eta)\zeta/\zeta_m}$. This yields

$$\psi_\eta = z\frac{\zeta_m}{\zeta} - 2. \tag{74}$$

E. An algorithm to estimate the effective coupling constants

In order to obtain the effective KPZ nonlinearity λ, one can tilt the system and estimate the change in the depinning force as in [48]. In contrast, the effective elasticity c has to our best knowledge never been estimated numerically. Since the field theory in Ref. [49] did not deliver an FRG fixed point for the ratio λ/c, we decided to check numerically whether such a fixed point exists, and to extract as much information as possible to constrain the field theory.

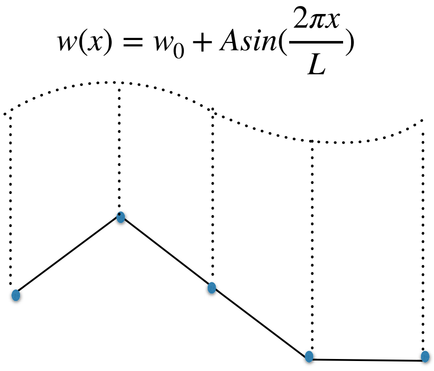

FIG. 14. We drive the interface with the spatially modulated driving given in Eq. (75), with $f = 1$. The continuous black line and the blue dots represent the interface, while the gray dashed line represents $w(x)$.

Our algorithm to achieve this is simple: measure the response of the interface to a perturbation, sinusoidal in space, and constant in time. This is achieved by driving the system with a spatially modulated background field $w(x)$ (see Fig. 14),

$$w(x) = w_0 + A\sin\left(f\frac{2\pi x}{L}\right). \tag{75}$$

After each avalanche, we increase $w(x)$ by δw (a constant), $w(x) \to w(x) + \delta w$. We focus on the slowest mode $f = 1$. We then measure the mean interface profile, i.e., its *response*, $\overline{u(x)}$. Varying the amplitude A of the driving, we fit this response with a polynomial in A. The effective parameters are then linked to the projections on these modes. To be specific, write, with $\ell := L/2\pi$,

$$\overline{u(x)} = u_0(A) + u_1(A)\sin\left(\frac{x}{\ell}\right) + u_2(A)\cos\left(\frac{2x}{\ell}\right) + \cdots, \tag{76}$$

$$u_0(A) = {}^0u_0 + {}^2u_0A^2 + \mathcal{O}(A^4), \tag{77}$$

$$u_1(A) = {}^1u_1A + \mathcal{O}(A^3), \tag{78}$$

$$u_2(A) = {}^2u_2A^2 + \mathcal{O}(A^4). \tag{79}$$

The dots represent higher-order terms in A, while the double-indexed u's are numbers to be estimated numerically. The lower index represents the mode, while the upper index is the order in A. We inject this development into the noiseless KPZ equation

$$-m^2u + c\nabla^2u + \lambda(\nabla u)^2 = -m^2A\sin\left(\frac{x}{\ell}\right). \tag{80}$$

It is the nonlinear term in this equation that generates the higher harmonics. The parity of the number of derivatives restricts the allowed modes to those in Eq. (76). Matching

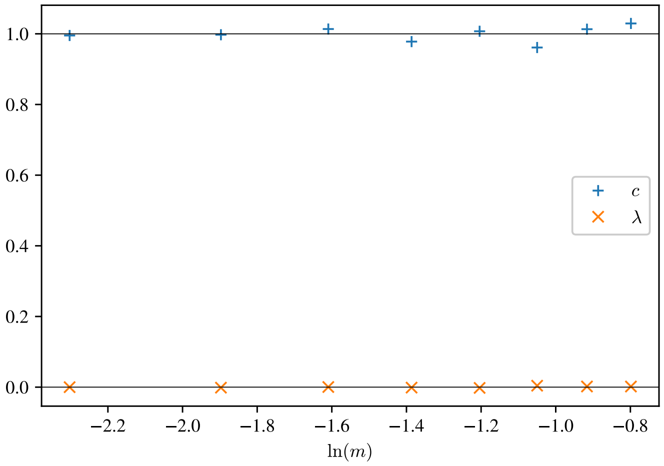

FIG. 15. The numerically estimated effective c and λ for the qEW equation. The effective elasticity c does not depend on m (with noticeable simulation errors at large m), as predicted by the statistical tilt symmetry (STS). The numerically estimated nonlinearity λ vanishes.

coefficients, we find

$$ {}^0u_0 = w_0, \tag{81} $$

$$ {}^1u_1 = \frac{m^2}{m^2 + \frac{c}{\ell^2}}, \tag{82} $$

$$ {}^2u_0 = \frac{m^2\lambda}{4\ell^2\left(m^2 + \frac{c}{\ell^2}\right)^2}, \tag{83} $$

$$ {}^2u_2 = \frac{m^4\lambda}{4\ell^2\left(m^2 + \frac{4c}{\ell^2}\right)\left(m^2 + \frac{c}{\ell^2}\right)^2}. \tag{84} $$

These relations are inverted to obtain λ and c,

$$ c(m) = m^2\ell^2\frac{1 - {}^1u_1}{{}^1u_1}, \tag{85} $$

$$ \lambda(m) = 4m^2\ell^2\frac{{}^2u_0}{({}^1u_1)^2}. \tag{86} $$

F. Tests and results

Let us start with some tests of our procedure for qEW. There $\lambda(m) \equiv 0$, and there is no renormalization of c, as it is protected by the statistical-tilt symmetry, the statistical invariance of the equation of motion under the transformation $u(x,t) \to u(x,t) + \alpha x$. In Fig. 15 we show simulations for harmonic depinning [Eq. (6) with $c_4 = 0$ and $c = 1$]. We estimated the effective elastic constant c, and see that it does not renormalize and stays at $c = 1$. Moreover, the numerically estimated $\lambda = 0$.

We next apply our procedure to TL92 and anharmonic depinning in $d = 1$; see Fig. 13. For each m, the polynomials were fitted on 100 different values for A, and each value of A corresponds to a simulation of 10^5 independent samples. The size varies from $L = 512$ to $L = 2048$, since for larger values of m smaller systems are sufficient. We find

$$ \psi_c^{d=1} = 1.31 \pm 0.04, \tag{87} $$

$$ \psi_\lambda^{d=1} = 0.28 \pm 0.03, \tag{88} $$

in agreement with their expressions in Eqs. (72) and (73), and the numerical values given in Table V.

We checked that higher-order relations (given in Appendix B) give the same values for c and λ. We further checked that the results given for λ are the same as those obtained as a response to a tilt. (Note that to introduce a tilt with our driving protocol, one has to tilt both the driving potential and the interface.)

The determination of the effective parameters λ and c is not the only application of this algorithm: one can numerically estimate the effective decay of subleading parameters present in the microscopic model, such as c_4, and obtain valuable information on the crossover to the qKPZ universality class. This may be helpful for experiments and is summarized in Appendix B. While many things can be numerically estimated, this technique is limited by the available computer resources, as illustrated in Fig. 19 for the decay of c_4.

G. The universal KPZ amplitude $\mathcal{A}$

An important question is whether qKPZ is the proper large-distance description of TL92, anharmonic depinning, and itself (i.e., a numerical implementation of the qKPZ equation). To ensure this, the properly renormalized nonlinearity λ needs to flow to a fixed point. While λ and c both flow, i.e., do not go to a fixed point by themselves, this is achieved by the *universal KPZ amplitude* $\mathcal{A}$,

$$ \mathcal{A} := \rho\frac{\lambda}{c}, \qquad \rho = \frac{\Delta(0)}{|\Delta'(0^+)|}. \tag{89} $$

The idea behind this construction is that if both λ and c are relevant, then

$$ \lambda[\nabla u(x,t)]^2 \sim c\nabla^2 u(x,t) \quad \Longrightarrow \quad \frac{\lambda}{c} \sim \frac{1}{u}. \tag{90} $$

On the other hand $\Delta(u) \sim u\Delta'(u)$, thus we can define a correlation length $\rho \sim u$ by $\rho := \Delta(0)/|\Delta'(0^+)|$; this allows one to write the dimensionless quantity $\mathcal{A}$ in Eq. (89). Note that the definition (89) ensures that $\mathcal{A}$ remains invariant under a change of units for u, say, from mm to km, and the same (independently) for x.

The reader may wonder whether our definition for $\mathcal{A}$ is unique? It is not, as one could instead of ρ use another characteristic scale, such as $\xi_\perp$. The reason we use ρ defined in Eq. (89) rather than $\xi_\perp$ defined in Eq. (33) is that the former is simpler to handle analytically.

If the qKPZ equation is the effective field theory in the limit of $m \to 0$, then the ratio $\mathcal{A}$ needs to converge to a universal limit set by the qKPZ field theory. That this is indeed the case can be seen in Fig. 13. In the two models simulated, the amplitude ratio converges to the same value,

$$ \mathcal{A}^{d=1} = 1.10(2). \tag{91} $$

Given that the microscopic models are quite different, this is a strong sign of universality.

H. Interpretation of $\mathcal{A}$: How strong is the KPZ nonlinearity?

The reader may ask himself whether the amplitude $\mathcal{A} = 1.1$ estimated numerically in Eq. (91) is small, or large:

first, it is definitely much larger than for qEW, for which $\mathcal{A}^{\rm qEW}=0$ (since $\lambda=0$ there).

For a rough estimate at the microscopic scale, we can convert the arguments of Sec. III C into a prediction for $\mathcal{A}$. Let us first consider the mapping of TL92 onto qKPZ, which resulted into the values for c and λ given in Eq. (22). If we take these values, and the lattice size $\rho=1$ for the correlation length of the disorder, then we get a microscopic or *bare* value of $\mathcal{A}$,

$$\mathcal{A}^{\rm bare}_{d=1}\approx\frac{5}{4}. \tag{92}$$

It is surprising that the estimate (92) at small scales is close to the large-scale estimate (91) of our numerical simulation.

Can one give a bound for $\mathcal{A}$, or could one have estimated an arbitrarily large value in Eq. (91)? Let us consider Fig. 3. We ask that in the absence of disorder the point N does not advance, thus F_N be negative. This means that the ratio between KPZ[1] and elastic term is bounded by 1,

$$1\geqslant\frac{\lambda(\nabla u)^2}{c|\nabla^2 u|}\simeq\frac{\lambda\left(\frac{\delta u}{2\xi_m}\right)^2}{c\left(\frac{\delta u}{\xi_m}\right)^2}=\frac{\lambda\delta u}{4c}. \tag{93}$$

We now need to estimate δu. Taking it as the typical fluctuation at scale ξ_m, i.e., the perpendicular correlation length $\xi_\perp$, gives $\delta u=\xi_\perp$ as defined in Sec. IV C. If this heuristic argument is correct, then

$$\mathcal{A}\lesssim\mathcal{A}^{\rm c}:=\frac{4\rho}{\xi_\perp}. \tag{94}$$

While $\mathcal{A}^{\rm c}$ is a bound on the value $\mathcal{A}$ can take before the interface becomes unstable, it is not necessarily the most stringent bound. In our simulations we find

$$\frac{\rho}{\xi_\perp}=0.85(1), \tag{95}$$

rather independent of m. This in turn gives

$$\mathcal{A}^{\rm c}_{d=1}=3.40(4). \tag{96}$$

Thus in $d=1$ the amplitude $\mathcal{A}$ is definitely large, though below its critical value. Field theory (see the companion paper [51]) gives a bound of $\mathcal{A}^{\rm c}_{d=1}=2$ (at leading order).

More intuition can be gotten from rescaling: If one uses the dimensionless variables $\tilde u:=\frac{u}{\rho}$, $\tilde w:=\frac{w}{\rho}$ and $\tilde x:=\frac{xm}{\sqrt{c}}$, then blocking configurations satisfy

$$0=\nabla^2\tilde u+\mathcal{A}(\nabla\tilde u)^2+\tilde w-\tilde u+\tilde F(\tilde x,\tilde u). \tag{97}$$

In these units, forces are correlated according to

$$\langle\tilde F(\tilde x,\tilde u)\tilde F(\tilde x',\tilde u')\rangle=\delta^d(\tilde x-\tilde x')\tilde\Delta(\tilde u-\tilde u'), \tag{98}$$

with

$$\tilde\Delta(\tilde u)=\frac{m^{d-4}}{c^{d/2}\rho^2}\Delta(\rho\tilde u). \tag{99}$$

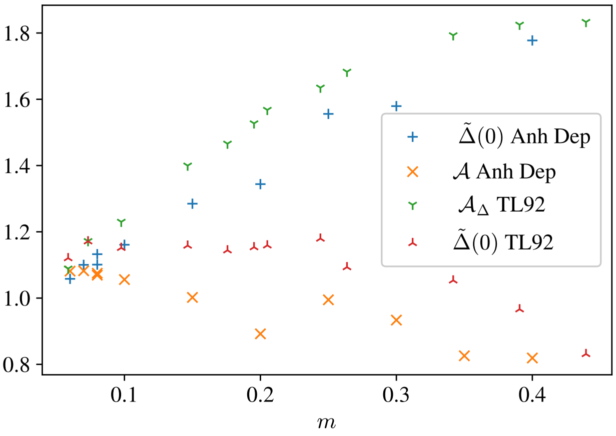

FIG. 16. $\tilde\Delta(0)$ and $\mathcal{A}$ for Anharmonic depinning and TL92 in $d=1$. They seem to converge to the same value for this particular scaling choice.

We estimate Eq. (99) in Fig. 16 for $d=1$, and find that $\tilde\Delta(0)\approx\mathcal{A}$. The conclusion is that at the critical point, at least in $d=1$, all parameters are of order one, and thus equally important.

VI. CONCLUSION

We showed through theoretical arguments and numerical tests that anharmonic depinning, qKPZ, and the cellular automaton TL92 are in the same universality class, the qKPZ universality class, for $d\leqslant 2$. For $2<d\leqslant 4$, there is evidence that TL92 may depart from the qKPZ universality class (which still includes anharmonic depinning at those dimensions).

We then elucidated the scaling relations for driving through a parabolic confining potential. This allowed us to understand statics and dynamics of qKPZ. Finally, we developed an algorithm to estimate the renormalized (effective) coefficients of the continuity equation. We find that, at least in $d=1$, all quantities are equally important, of order one in a particular scheme. Our work will be used to constrain and ultimately construct the field theory, which is presented in a sequel to this work [51].

We believe that our technique to extract the effective coupling constants by measuring the static response of the system under spatially modulated perturbations may yield important information in other systems that lack a proper field theoretic description. As an example, we started to extend our approach to the thermal KPZ equation.

ACKNOWLEDGMENTS

We thank Alberto Rosso for useful discussions. J.A.B. acknowledges support from NSF Grant No. DMS-2052616. M.A.M. acknowledges financial support from the Spanish Ministry and Agencia Estatal de Investigación (AEI) through Project I+D+i Ref. PID2020-113681GB-I00, financed by MICIN/AEI/10.13039/501100011033 and FEDER "A Way to Make Europe."

---

[1] Note that the discretization (5) for the KPZ term induces a numerical factor of $1/4$ into the equation. Given that these values for λ and c are effective large-scale estimates, this factor should be taken with a grain of salt.

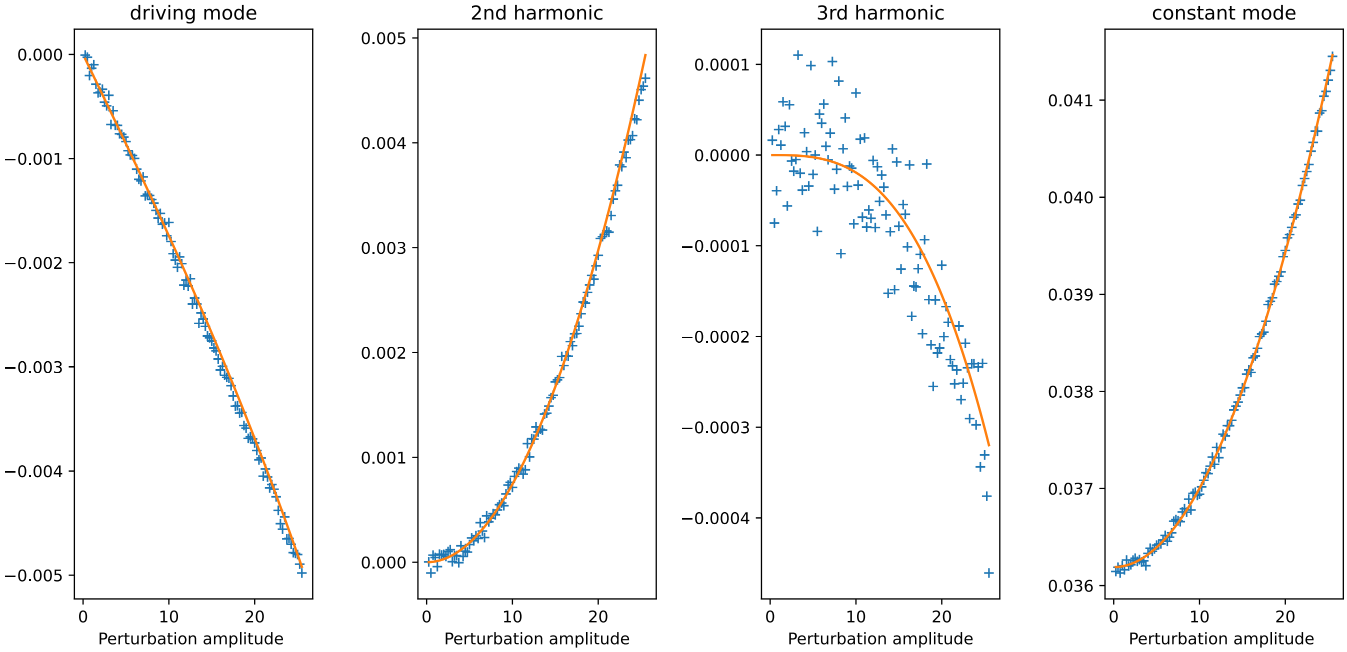

FIG. 17. Numerical estimation of the interface modes for different driving amplitude A. From the orange fits one obtains the coefficients ${}^{i}u_j$ defined in Eqs. (76)–(79). For example, from the fit of the driving mode one obtains ${}^{1}u_1$ and ${}^{3}u_1$. The polynomial behavior predicted in Eq. (79) is verified. The shown plots are for anharmonic depinning, $L = 1024$, and $m = 0.06$. The perturbation amplitude is in lattice units.

APPENDIX A: WHY $z \neq 1$

In Ref. [5] the authors provide a heuristic argument for $z = 1$ in $d = 1$, while for a higher dimension they conjecture that $z = d_{\min}$ with $d_{\min}$ the exponent on how the shortest-path length on a d-dimensional critical percolating cluster scales with the Euclidean distance. Our simulations invalidate this heuristics. Here we give theoretical arguments as to why this heuristics fails. Ref. [5] studies TL92 with parallel updates. After an avalanche, they define the path of invaded cells as the path (in one dimension) from the cell from which it was invaded to the cell it invaded. Then they assert that the path length from the start of the avalanche to site i is equal to the time it took for cell i to be invaded. Then z is defined by $T \sim \ell^z$ with T the avalanche duration and ℓ the lateral extension of the avalanche. Since $\xi_\perp/\xi_m \to 0$, the invading path is considered rough as the path along the blocking configuration, so $\ell \approx \xi_m$. As a result they find $z = 1$. However, equating the length of the invading path with the duration of an avalanche is problematic: After reaching site i, the avalanche can change direction and then come back, and as a result the duration is underestimated, and $z > 1$.

In higher dimensions, this underestimation persists, but is associated with another problem, that overestimates z: since $\xi_\perp/\xi_m \to 0$ they model the $d+1$-dimensional space in which the invading path lives as a d-dimensional critical percolation cluster, and then declare the invading path to be the shortest distance between two points on this percolation cluster. However, the transport properties of percolation clusters are highly dependent on the proportion of singly connected cells [62] (i.e., cells that if removed separate the percolation cluster in two). The existence of another dimension through which the path can go changes the statistics of those singly connected cells. There are far more ways to reach one target, and as a result the time it takes to reach it may be smaller and z overestimated.

APPENDIX B: DETAILS OF THE ALGORITHM

1. Numerical details

In Fig. 17 we show the results of measuring the modes of the interface for different amplitudes of the driving. One has to be careful to be in the small-perturbation limit. We find that taking the maximum perturbation amplitude to be $A = \frac{L}{40}$ to be appropriate. The number of points needed within that range to have a good precision on the polynomial fit is hard to deduce in advance and varies with m. We find that sometimes the small perturbation limit is reached before $A = \frac{L}{40}$ and in that case it is good to have more points in order to maintain a good fit for the polynomials. A good rule of thumb is to have around 50 points.

2. Higher-order relations

There are higher order relations for λ and c. Here we put them, for completeness:

$$c(m) = \left(\frac{{}^{2}u_0}{{}^{2}u_2} - 1\right)\frac{m^2\ell^2}{4}, \tag{B1}$$

$$\lambda(m) = \frac{4\ell^2}{m^4}\left(m^2 + \frac{4c}{\ell^2}\right)\left(m^2 + \frac{c}{\ell^2}\right)^2 {}^{2}u_2. \tag{B2}$$

In Fig. 18 we can see that for smaller m, the higher order formulas agrees with their lower order counterpart. For higher m the signal for c determined with Eq. (B2) is too noisy. For λ there is good agreement for all m.

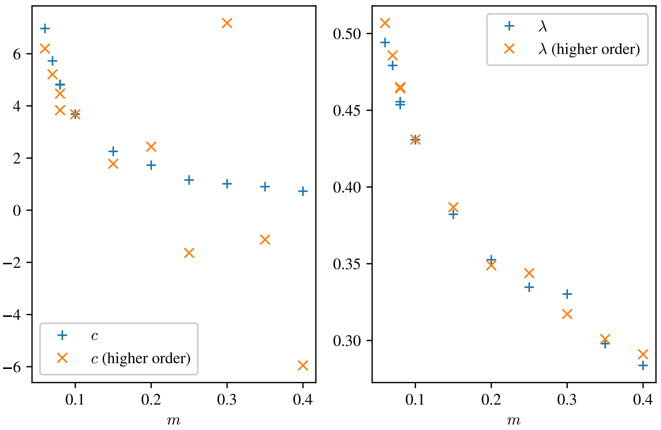

FIG. 18. Comparison of the different formulas (Eq. (86) and Eq. (B2) for a fit based on higher-order harmonics) for determining c and λ, for aDep in $d = 1$. We see a good agreement for λ, while for c the higher-order harmonics are too noisy for $m \geqslant 0.2$.

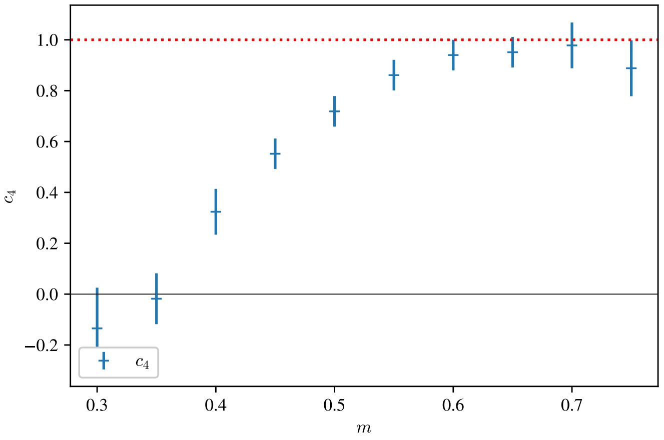

FIG. 19. Numerically estimated effective anharmonicity c_4 determined for anharmonic depinning using Eq. (B3). $L = 64$ and the initial condition is $c_4 = 1$ (red dotted line). The numerically estimated effective c_4 decreases as m decreases, vanishing within the precision of our simulation when $m \approx 0.3$. There the error for c_4 increases, as the small system sees more system-spanning avalanches, crossing over to a single-particle behavior. Increasing L further increases this error, since c_4 is determined through a high-order harmonics of the driving signal, and scales $\sim L^4$ appearing in Eq. (B3). Still, qualitatively this confirms that c_4 can be dropped in the effective long-distance description of the model.

3. Crossover and higher-order anharmonic terms

An interesting question is the crossover from the microscopic model, e.g., in anharmonic depinning which contains a coefficient c_4. How does this terms decrease with m? To answer these questions, we derive a formula for the expression of c_4. If a c_4 term is present, then the lowest order in A is A^3. We find that there is a contribution of c_4 on the first mode, written for compactness in terms of ${}^j u_i$, λ, and c,

$$c_4(m) = -4\frac{\ell^4}{({}^1u_1)^3}\left[\frac{\lambda\,{}^1u_1\,{}^2u_2}{\ell^2} + {}^3u_1\left(m^2 + \frac{c}{\ell^2}\right)\right]. \tag{B3}$$

c_4 appears as a third-order perturbation in A. Since it comes from higher harmonics, it is more heavily suppressed as the system becomes larger. As a result, small system sizes (and large m) must be considered to accurately estimate c_4. However, there is a tradeoff, since c and λ are determined with a lesser accuracy for smaller systems size. The result for an initial anharmonic depinning equation with $c_4 = 1$ are presented in Fig. 19. We see that at large m the microscopic value $c_4 = 1$ is obtained. Reducing m to about 0.35, the effective c_4 becomes too small to be distinguishable from the noise.

[1] T. Giamarchi and P. Le Doussal, Elastic theory of flux lattices in the presence of weak disorder, Phys. Rev. B **52**, 1242 (1995).

[2] J. A. Bonachela, C. D. Nadell, J. B. Xavier, and S. A. Levin, Universality in bacterial colonies, J. Stat. Phys. **144**, 303 (2011).

[3] M. A. C. Huergo, N. E. Muzzio, M. A. Pasquale, P. H. Pedro González, A. E. Bolzán, and A. J. Arvia, Dynamic scaling analysis of two-dimensional cell colony fronts in a gel medium: A biological system approaching a quenched Kardar-Parisi-Zhang universality, Phys. Rev. E **90**, 022706 (2014).

[4] M. Alava and M. A. Muñoz, Interface depinning versus absorbing-state phase transitions, Phys. Rev. E **65**, 026145 (2002).

[5] L. A. N. Amaral, A.-L. Barabási, S. V. Buldyrev, S. T. Harrington, S. Havlin, R. Sadr-Lahijany, and H. E. Stanley, Avalanches and the directed percolation depinning model: Experiments, simulations, and theory, Phys. Rev. E **51**, 4655 (1995).

[6] R. Planet, L. Díaz-Piola, and J. Ortín, Capillary jumps of fluid-fluid fronts across an elementary constriction in a model open fracture, Phys. Rev. Fluids **5**, 044002 (2020).

[7] R. Holtzman, M. Dentz, R. Planet, and J. Ortín, The origin of hysteresis and memory of two-phase flow in disordered media, Commun. Phys. **3**, 222 (2020).

[8] K. J. Wiese, Theory and experiments for disordered elastic manifolds, depinning, avalanches, and sandpiles, Rep. Prog. Phys. **85**, 086502 (2022).

[9] H. Hinrichsen, Non-equilibrium critical phenomena and phase transitions into absorbing states, Adv. Phys. **49**, 815 (2000).

[10] D. S. Fisher, Interface Fluctuations in Disordered Systems: $5-\varepsilon$ Expansion and Failure of Dimensional Reduction, Phys. Rev. Lett. **56**, 1964 (1986).

[11] O. Narayan and D. S. Fisher, Threshold critical dynamics of driven interfaces in random media, Phys. Rev. B **48**, 7030 (1993).

[12] T. Nattermann, S. Stepanow, L.-H. Tang, and H. Leschhorn, Dynamics of interface depinning in a disordered medium, J. Phys. II France **2**, 1483 (1992).

[13] H. Leschhorn, T. Nattermann, S. Stepanow, and L.-H. Tang, Driven interface depinning in a disordered medium, Ann. Phys. **509**, 1 (1997).

[14] P. Chauve, P. Le Doussal, and K. J. Wiese, Renormalization of Pinned Elastic Systems: How Does It Work beyond One Loop? Phys. Rev. Lett. **86**, 1785 (2001).
[15] P. Le Doussal, K. J. Wiese, and P. Chauve, Two-loop functional renormalization group analysis of the depinning transition, Phys. Rev. B **66**, 174201 (2002).
[16] P. Le Doussal, K. J. Wiese, and P. Chauve, Functional renormalization group and the field theory of disordered elastic systems, Phys. Rev. E **69**, 026112 (2004).
[17] J. P. Sethna, K. A. Dahmen, and C. R. Myers, Crackling noise, Nature (London) **410**, 242 (2001).
[18] A. Rosso, P. Le Doussal, and K. J. Wiese, Avalanche-size distribution at the depinning transition: A numerical test of the theory, Phys. Rev. B **80**, 144204 (2009).
[19] P. Le Doussal and K. J. Wiese, Size distributions of shocks and static avalanches from the functional renormalization group, Phys. Rev. E **79**, 051106 (2009).
[20] P. Le Doussal, A. A. Middleton, and K. J. Wiese, Statistics of static avalanches in a random pinning landscape, Phys. Rev. E **79**, 050101(R) (2009).
[21] P. Le Doussal, M. Müller, and K. J. Wiese, Avalanches in mean-field models and the Barkhausen noise in spin-glasses, Europhys. Lett. **91**, 57004 (2010).
[22] P. Le Doussal and K. J. Wiese, Elasticity of a contact-line and avalanche-size distribution at depinning, Phys. Rev. E **82**, 011108 (2010).
[23] P. Le Doussal and K. J. Wiese, First-principle derivation of static avalanche-size distribution, Phys. Rev. E **85**, 061102 (2012).
[24] P. Le Doussal, M. Müller, and K. J. Wiese, Equilibrium avalanches in spin glasses, Phys. Rev. B **85**, 214402 (2012).
[25] P. Le Doussal and K. J. Wiese, Avalanche dynamics of elastic interfaces, Phys. Rev. E **88**, 022106 (2013).
[26] A. Dobrinevski, P. Le Doussal, and K. J. Wiese, Statistics of avalanches with relaxation and Barkhausen noise: A solvable model, Phys. Rev. E **88**, 032106 (2013).
[27] A. Dobrinevski, P. Le Doussal, and K. J. Wiese, Avalanche shape and exponents beyond mean-field theory, Europhys. Lett. **108**, 66002 (2014).
[28] T. Thiery, P. Le Doussal, and K. J. Wiese, Spatial shape of avalanches in the Brownian force model, J. Stat. Mech. (2015) P08019.
[29] L. E. Aragon, A. B. Kolton, P. Le Doussal, K. J. Wiese, and E. Jagla, Avalanches in tip-driven interfaces in random media, Europhys. Lett. **113**, 10002 (2016).
[30] M. Delorme, P. Le Doussal, and K. J. Wiese, Distribution of joint local and total size and of extension for avalanches in the Brownian force model, Phys. Rev. E **93**, 052142 (2016).
[31] G. Durin, F. Bohn, M. A. Correa, R. L. Sommer, P. Le Doussal, and K. J. Wiese, Quantitative Scaling of Magnetic Avalanches, Phys. Rev. Lett. **117**, 087201 (2016).
[32] T. Thiery, P. Le Doussal, and K. J. Wiese, Universal correlations between shocks in the ground state of elastic interfaces in disordered media, Phys. Rev. E **94**, 012110 (2016).
[33] Z. Zhu and K. J. Wiese, The spatial shape of avalanches, Phys. Rev. E **96**, 062116 (2017).
[34] J. A. Bonachela, M. Alava, and M. A. Muñoz, Cusps in systems with (many) absorbing states, Phys. Rev. E **79**, 050106 (2009)(R).
[35] P. Le Doussal and K. J. Wiese, How to measure functional RG fixed-point functions for dynamics and at depinning, Europhys. Lett. **77**, 66001 (2007).
[36] A. A. Middleton, P. Le Doussal, and K. J. Wiese, Measuring Functional Renormalization Group Fixed-Point Functions for Pinned Manifolds, Phys. Rev. Lett. **98**, 155701 (2007).
[37] P. Le Doussal, K. J. Wiese, S. Moulinet, and E. Rolley, Height fluctuations of a contact line: A direct measurement of the renormalized disorder correlator, Europhys. Lett. **87**, 56001 (2009).
[38] K. J. Wiese, M. Bercy, L. Melkonyan, and T. Bizebard, Universal force correlations in an RNA-DNA unzipping experiment, Phys. Rev. Res. **2**, 043385 (2020).
[39] C. ter Burg, F. Bohn, F. Durin, R. L. Sommer, and K. J. Wiese, Force Correlations in Disordered Magnets, Phys. Rev. Lett. **129**, 107205 (2022).
[40] L.-H. Tang and H. Leschhorn, Pinning by directed percolation, Phys. Rev. A **45**, R8309 (1992).
[41] S. V. Buldyrev, A.-L. Barabasi, F. Caserta, S. Havlin, H. E. Stanley, and T. Vicsek, Anomalous interface roughening in porous media: Experiment and model, Phys. Rev. A **45**, R8313 (1992).
[42] S. V. Buldyrev, S. Havlin, and H. E. Stanley, Anisotropic percolation and the d-dimensional surface roughening problem, Physica A **200**, 200 (1993).
[43] M. Kardar, G. Parisi, and Y.-C. Zhang, Dynamic Scaling of Growing Interfaces, Phys. Rev. Lett. **56**, 889 (1986).
[44] S. Atis, A. K. Dubey, D. Salin, L. Talon, P. Le Doussal, and K. J. Wiese, Experimental Evidence for Three Universality Classes for Reaction Fronts in Disordered Flows, Phys. Rev. Lett. **114**, 234502 (2015).
[45] T. Chevalier, A. K. Dubey, S. Atis, A. Rosso, D. Salin, and L. Talon, Avalanches dynamics in reaction fronts in disordered flows, Phys. Rev. E **95**, 042210 (2017).
[46] P. Grassberger, Morphological transitions in supercritical generalized percolation and moving interfaces in media with frozen randomness, Phys. Rev. Res. **2**, 043150 (2020).
[47] A. Rosso, A. K. Hartmann, and W. Krauth, Depinning of elastic manifolds, Phys. Rev. E **67**, 021602 (2003).
[48] L.-H. Tang, M. Kardar, and D. Dhar, Driven Depinning in Anisotropic Media, Phys. Rev. Lett. **74**, 920 (1995).
[49] P. Le Doussal and K. J. Wiese, Functional renormalization group for anisotropic depinning and relation to branching processes, Phys. Rev. E **67**, 016121 (2003).
[50] I. Jensen, Critical Behavior of the Pair Contact Process, Phys. Rev. Lett. **70**, 1465 (1993).
[51] G. Mukerjee and K. J. Wiese, Depinning in the quenched Kardar-Parisi-Zhang class. II. Field theory, Phys. Rev. E **107**, 054137 (2023).
[52] K. Sneppen, Self-Organized Pinning and Interface Growth in a Random Medium, Phys. Rev. Lett. **69**, 3539 (1992).
[53] B. Moglia, E. V. Albano, P. Villegas, and M. A. Muñoz, Interfacial depinning transitions in disordered media: Revisiting an old puzzle, J. Stat. Mech. (2014) P10024.
[54] C. Lee and J. M. Kim, Depinning transition of the quenched Kardar-Parisi-Zhang equation, J. Korean Phys. Soc. **47**, 13 (2005).
[55] A. A. Middleton, Asymptotic Uniqueness of the Sliding State for Charge-Density Waves, Phys. Rev. Lett. **68**, 670 (1992).

[56] A. Rosso and W. Krauth, Origin of the Roughness Exponent in Elastic Strings at the Depinning Threshold, Phys. Rev. Lett. **87**, 187002 (2001).

[57] N. Araújo, P. Grassberger, B. Kahng, K. J. Schrenk, and R. M. Ziff, Recent advances and open challenges in percolation, Eur. Phys. J. Spec. Top. **223**, 2307 (2014).

[58] D. Dhar, Directed percolation and directed animals, arXiv:1703.07541.

[59] A.-L. Barabasi, G. Grinstein, and M. A. Muñoz, Directed Surfaces in Disordered Media, Phys. Rev. Lett. **76**, 1481 (1996).

[60] E. E. Ferrero, S. Bustingorry, and A. B. Kolton, Non-steady relaxation and critical exponents at the depinning transition, Phys. Rev. E **87**, 032122 (2013).

[61] P. Grassberger, D. Dhar, and P. K. Mohanty, Oslo model, hyperuniformity, and the quenched Edwards-Wilkinson model, Phys. Rev. E **94**, 042314 (2016).

[62] D. Stauffer and A. A. Aharony, *An Introduction to Percolation Theory* (Taylor & Francis, London, 1994).

[63] Y.-J. Chen, S. Papanikolaou, J. P. Sethna, S. Zapperi, and G. Durin, Avalanche spatial structure and multivariable scaling functions: Sizes, heights, widths, and views through windows, Phys. Rev. E **84**, 061103 (2011).

[64] A. Kolton, P. Le Doussal, and K. J. Wiese, Distribution of velocities in an avalanche, and related quantities: Theory and numerical verification, Europhys. Lett. **127**, 46001 (2019).

[65] A. Rosso and W. Krauth, Monte Carlo dynamics of driven strings in disordered media, Phys. Rev. B **65**, 012202 (2001).